Received: 25 May 2021 | Revised: 9 November 2021 | Accepted: 11 November 2021

DOI: 10.1002/met.2037

Meteorological Applications
Science and Technology for Weather and Climate
Open Access
RMetS

RESEARCH ARTICLE

# Nocturnal atmospheric conditions and their impact on air pollutant concentrations in the city of Stuttgart

**Olga Kiseleva**[1] | **Norbert Kalthoff**[1] | **Bianca Adler**[2,3] | **Meinolf Kossmann**[4] | **Andreas Wieser**[1] | **Rayk Rinke**[5]

[1]Institute of Meteorology and Climate Research—Department of Troposphere Research (IMK-TRO), Karlsruhe Institute of Technology (KIT), Karlsruhe, Germany

[2]CIRES, University of Colorado, Boulder, Colorado, USA

[3]NOAA Physical Sciences Laboratory, Boulder, Colorado, USA

[4]Climate and Environment Consultancy, Deutscher Wetterdienst, Offenbach am Main, Germany

[5]Stadt Stuttgart, Amt für Umweltschutz, Abteilung Stadtklimatologie, Stuttgart, Germany

**Correspondence**
Olga Kiseleva, Institute of Meteorology and Climate Research—Department Troposphere Research (IMK-TRO), Karlsruhe Institute of Technology, Hermann-von-Helmholtz-Platz 1, 76344 Eggenstein-Leopoldshafen, P.O. Box 3640, 76021 Karlsruhe, Germany.
Email: olga.kiseleva@kit.edu

**Funding information**
German Federal Ministry of Education and Research (BMBF) under grants 01LP1602 G and 01LP1602 K within the research programme [UC]$^2$.

## Abstract

Meteorological and air pollutant measurements were conducted in the area of Stuttgart during winter and summer seasons. Stuttgart is situated in moderate mountainous terrain in southwestern Germany. We focus on the connection between atmospheric conditions and air pollutants in the urban nocturnal boundary layer. This is done by relating the bulk Richardson number (Rib), turbulence intensity, cloudiness, and winds, as well as $NO_x$ and $O_3$ data. Turbulence intensity is inversely related to Rib, with the lower values occurring at Rib >0.33. The coefficient of determination for the exponential regression is only moderate, which partly can be attributed to sporadic turbulence in the transition from dynamically unstable to stable flows. Dynamically unstable flows (Rib <0.33) occur frequently in winter, as a result of the presence of low-level clouds and strong winds, supporting low buoyant suppression and strong shear generation of turbulence. Dynamically stable flows (Rib >1.25) are found preferably under clear skies in summer with the build-up of strong surface inversions, so that buoyant suppression is strong and shear generation of turbulence is weak. The nocturnal $NO_x$ concentrations are positively correlated with Rib. The correlation is weak, which is mainly related to the large variability of air pollutant concentrations in a range around Rib = 0.33. In this range, many low-level jets are present that can cause sporadic turbulent coupling between the atmosphere and the surface. Reduced mixing under dynamically stable flows causes $NO_x$ values about 3 times higher than under dynamically unstable flows. The overall lowest $NO_x$ concentrations occur during winter when low clouds and strong winds are present.

**KEYWORDS**

[UC]$^2$, complex terrain, low-level jet, $NO_x$, $O_3$, surface inversion, TKE

## 1 | INTRODUCTION

Air quality is a well-known issue in many populated areas of the world. Besides the emission strength of air pollutants, the wind speed and atmospheric stratification determine the air quality considerably. Factors influencing the atmospheric stratification are boundary conditions such as the synoptic conditions and land-surface

properties. Parameters such as the Richardson number are often used to quantify the atmospheric stratification and to indicate whether turbulence can exist (e.g., Stull, 1988). In the nocturnal boundary layer (NBL), the suppression of turbulence is affected by the formation of surface temperature inversions built under weak synoptic forcing and clear skies. The interplay between inversion-related suppression and shear generation of turbulence during the night, for example, due to a low-level jet (LLJ), was found to result in episodes with enhanced, intermittent vertical turbulent mixing of momentum, heat, and air constituents in the NBL (Corsmeier et al., 1997, 2006; Hu et al., 2013; Mathieu et al., 2005; Reitebuch et al., 2000; Salmond & McKendry, 2002).

Over complex terrain, mesoscale atmospheric phenomena additionally become important to air quality, because in valleys, slope and valley winds can effectively transport air pollutants (Kalthoff et al., 2000; Steyn et al., 2013; Zardi & Whiteman, 2013). Kossmann et al. (1998), S. F. J De Wekker and Kossmann (2015), and Rotach et al. (2015) described and reviewed most of these mechanisms active over mountainous terrain. Especially, cities located in valleys or basins are prone to high air pollutant concentrations (S. F. De Wekker et al., 2018; Fast & Zhong, 1998; Mayer, 1999; Panday & Prinn, 2009; Wanner & Hertig, 1984). This happens when unfavourable atmospheric conditions, such as cold pools, and high emissions, for example, from traffic, industrial activities, and domestic heating, occur simultaneously (Conangla et al., 2018; Whiteman et al., 1999).

The forecast of situations such as these is still a great challenge (e.g., Giovannini et al., 2020), and several field campaigns have been performed to improve the understanding of the interaction of nocturnal concentrations of pollutants with the vertical structure of the lower troposphere and/or to provide appropriate data for model validation (Doran et al., 2002; Lareau et al., 2013; Pardyjak et al., 2009; Price et al., 2011; Zhong & Fast, 2003). Tethered balloons (Glaser et al., 2003; Güsten et al., 1998; Pisano et al., 1997), radiosondes (Corsmeier et al., 2006), and meteorological towers (Li et al., 2005; Mathieu et al., 2005) have been used in this context. These studies have shown a strong dependence of air pollutants on the thermodynamic structures and turbulence processes in the NBL. However, tethered-balloon measurements usually are conducted during short, intensive observational periods and under moderate wind speeds. Tower measurements have limitations in vertical resolution and extension. Radiosondes are rarely launched at night.

A recently launched project, which fosters both field campaigns and the development of the parallelized large-eddy simulation model (PALM-4U, Maronga et al., 2019) to improve the understanding of city climates, is the German project 'Urban Climate Under Change' or $[UC]^2$ for short (Scherer, Ament, et al., 2019b; Scherer, Florian, et al., 2019a). One of the selected cities for these investigations is Stuttgart, a city well known for its air quality problems for many years (Mayer, 1999). Stuttgart is situated in a basin-shaped valley (Stuttgart basin), which opens into the Neckar valley in the northeast (Figure 1). This complex environment makes Stuttgart predestined for studying the connection between the state of the atmospheric boundary layer (ABL) and air pollutant concentrations. Within the framework of the $[UC]^2$ project, parts of the mobile integrated atmospheric observation platform KITcube (Kalthoff et al., 2013) were installed in the city of Stuttgart in 2017 and 2018 to collect a comprehensive data set pertaining to these connections. The data set, consisting of radiosonde and continuous, high-resolution wind lidar observations, has already allowed the successful study of the horizontal (Adler et al., 2020)

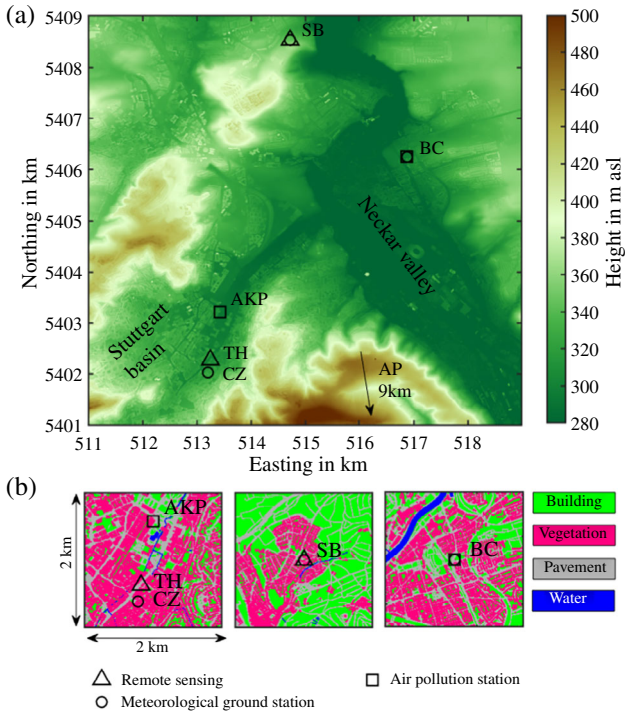


**FIGURE 1** (a) Topography (orography plus buildings) and measurement sites in and around the city of Stuttgart. Wind lidar and MWR were positioned on top of the town hall (TH). Radiosonde and ceilometer data are available at Schnarrenberg (SB). Near-surface meteorological observations were performed at the City Centre (CZ), Bad Cannstatt (BC), SB, and Stuttgart airport (AP). Air quality was measured at Arnulf-Klett Platz (AKP) and BC. (b) Maps with land use in the surroundings of the measurement sites. Topographic and land-use data are provided by the German aerospace Centre (DLR). Coordinate system: UTM (ETRS89) zone 32U, geoid egm2008

and vertical structure (Wittkamp et al., 2021) of the wind field in Stuttgart and its surroundings. In this study, we focus on the examination of the characteristics of the NBL, its relation to cloudiness and winds, and on the conditions aloft in the NBL and the associated near-surface air pollutant concentrations ($NO_x = NO + NO_2$; and $O_3$) both for winter and summer episodes. The atmospheric variables and processes under investigation are shown in the rectangles in Figure 2, and the connections between these are addressed through the following research questions:

1. What is the state of the NBL with respect to atmospheric stratification and how is it related to shear generation and buoyant suppression of turbulence both for summer and winter?
2. Do we see a connection between cloudiness and winds and the processes determining the atmospheric stratification?
3. How do cloudiness and winds impact the atmospheric stratification?
4. How does the observed turbulence intensity in the NBL relate to the atmospheric stratification?
5. How do the nocturnal near-surface $NO_x$ and $O_3$ concentrations relate to the atmospheric stratification and how does the relationship vary between different urban sites and between summer and winter nights?

The rest of the paper is structured as follows: Section 2 introduces the investigation area, measurement set-up, instrumentation, and available data. Section 3 describes the analysis methods. Atmospheric state, the relationships between atmospheric stratification, cloudiness and winds, and turbulence are analysed in Section 4 and for air pollutants in Section 5. In Section 6, two case studies from summer and winter episodes with dynamically stable and unstable flows, respectively, are presented. And finally, Section 7 summarizes the main findings.

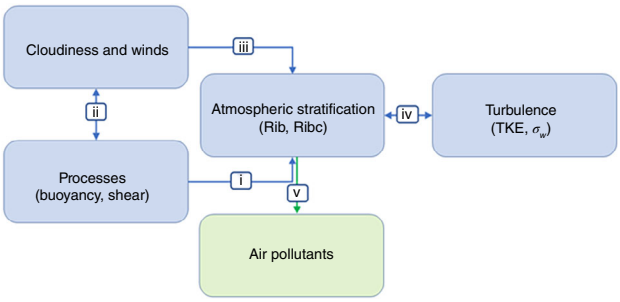


FIGURE 2 Schematic view of the research items outlined in Section 1. (1) Atmospheric state and impact of buoyant suppression and shear generation of turbulence on atmospheric stratification, (2) relation between cloudiness and winds and stratification-related processes, (3) impact of cloudiness and winds on atmospheric stratification, (4) connection between observed turbulence and Rib, and (5) influence of atmospheric stratification on air pollutants

## 2 | INVESTIGATION AREA, INSTRUMENT SET-UP, AND AVAILABLE DATA

### 2.1 | Investigation area and measurement campaigns

This study is based on a data set collected over the orographically structured terrain characterizing the surroundings of the city of Stuttgart in southwestern Germany (Figure 1). The area of interest includes the relatively broad Neckar valley (width about 2 km), which is orientated from southeast to northwest, and the basin-shaped valley called the Stuttgart basin (about 2.5 km $\times$ 2.5 km), which opens to the Neckar valley in the northeast. The valley floor is approximately at an altitude of 300 m above mean sea level (m asl) and surrounded by hills with ridge heights up to 520 m asl. The two observation periods used in this study lasted from 1 February to 31 March 2017 (winter campaign) and from 14 June to 31 August 2018 (summer campaign). In this study, we used meteorological data from the stations City Centre (CZ, 300 m asl) in the Stuttgart basin; Bad Cannstatt (BC, 303 m asl) and Schnarrenberg (SB, 366 m asl) in the Neckar valley, and Stuttgart Airport (AP, 411 m asl) on the Filder plateau. Air pollutant data were collected from the stations Arnulf-Klett Platz (AKP, 295 m asl) in the Stuttgart basin and Bad Cannstatt, and vertical profiling data from the stations Town Hall (TH, 297 m asl) in the Stuttgart basin and Schnarrenberg (Figure 1, Table 1). For a detailed overview of the measurement campaigns, we refer to Scherer, Ament, et al. (2019b).

### 2.2 | Vertical profiling of meteorological parameters

The remote sensing systems included one wind lidar of type Leosphere Windcube WLS8-3 (wind lidar) using a wavelength of 1.543 µm, pulse energy of 200 µJ, and pulse repetition frequency of 20 kHz; one ceilometer of type CHM15k Nimbus manufactured by Lufft (ceilometer) using a wavelength of 1.064 µm, pulse energy of 7–8 µJ, and repetition frequency of 5–7 kHz (Martucci et al. (2010); one scanning microwave radiometer (MWR) of type HATPRO RPG manufactured by Radiometer Physics (Rose et al., 2005); and the radiosonde system RS92 (winter campaign 2017) or RS41 (summer

**TABLE 1** Region, station name and applied abbreviation, measured parameters, and profiling instrument

| Region | Station name elevation (m asl/m agl) | Abbreviation | Measured chemical parameters | Measured meteorological parameters | Profiling instrument elevation (m asl/m agl) |
|---|---|---|---|---|---|
| Stuttgart basin | Arnulf-Klett Platz (295) 513276E, 5403366N | AKP | $NO_2$, NO, $O_3$ | | |
| | Town hall (297) 513099E, 5402426N | TH | | | MWR (297/60) Wind lidar (297/28) |
| | City centre (300/25) 513054E, 5402180N | CZ | | T, p, RH, \|v\|, wd | |
| Neckar valley | Bad Cannstatt (303) 516877E, 5406242N | BC | $NO_2$, NO, $O_3$ | G, T, p, RH, \|v\|, wd | |
| | Schnarrenberg (366) 514679E, 5408377N | SB | | G, T, p, RH, \|v\|, wd | Ceilometer (366) Radiosonde (366) |
| Filder plateau | Airport (411) 517696E, 5393083N | AP | | T, p, RH, \|v\|, wd | |

*Note*: G is solar irradiation, T is temperature, p is air pressure, RH is relative humidity, |v| is wind speed, and wd is wind direction. All instruments are installed at the ground except where indicated. For these, the height above ground level at which the instrument was deployed is added. Locations are given using UTM coordinates zone 32U.

campaign 2018) from Vaisala. The wind lidar and the MWR are part of the KITcube (Kalthoff et al., 2013) and were operated by the Karlsruhe Institute of Technology (KIT). These devices were placed on the rooftops of two buildings of the Town Hall (Figure 1) in the Stuttgart basin, that is, the MWR at 60 m above ground level (agl) (357 m asl) and the wind lidar at 28 m agl (325 m asl). The ceilometer and the radio-sounding system employed in this study were operated by the German Meteorological Service (DWD) at SB.

The wind lidar was operated alternately in two modes: the Doppler beam swing (DBS) mode, and the vertical stare mode. Using the DBS mode, the wind lidar performed measurements of radial wind speeds with a cone angle of 14.84° along the four beam directions of 90°, 180°, 270°, and 360°. It took the wind lidar 7 s to collect data at each beam location and to steer the beam to the next beam location. The 3D wind components were derived with a vertical resolution of 20 m from 40 m up to a maximum of 600 m above the roof level (depending on the aerosol concentration) and with a temporal resolution of 10 min from instantaneous radial velocities measured at each beam position by the internal software provided by Leosphere. According to the manufacturer's technical specifications, the accuracy of the wind speed is 0.2 m $s^{-1}$ and of wind direction is 1.5°. Using the vertical stare mode, the wind lidar beam was continuously pointing vertically, which provided a direct measurement of the vertical wind speed with a time resolution of 7 s.

The MWR was used to derive the vertical temperature profiles. These profiles were retrieved from brightness temperature measurements in the V-band using a retrieval algorithm provided by the University of Cologne (Löhnert et al., 2009; Löhnert & Crewell, 2003). Temperature profiles were retrieved every 15 min with a vertical resolution of 50 m up to 250 m over the device, increasing toward 200 m at 2000 m over the device. By combing the brightness temperature measurement from the zenith and from the low-elevation boundary layer scans, the accuracy of the temperature profiles in the ABL is improved to about <1 K (Crewell & Löhnert, 2007). Potential temperature profiles were calculated from temperature and pressure profiles. The pressure profiles were determined from in situ pressure measurements at the MWR's housing using the barometric equation.

Operational radio soundings were performed at Schnarrenberg twice a day reaching up to about 32 km asl with a vertical resolution of 10 m, providing profiles of air temperature, relative humidity, wind speed, wind direction, and air pressure (uncertainty of wind speed is 0.15 m $s^{-1}$ and of wind direction is 2°, and the total accuracy of temperature in the ABL is <0.5 K). The balloon was launched approximately 75 min before 00:00 and 12:00 Universal Standard Time (UTC), that is, at 22:45 and 10:45 UTC, respectively.

The ceilometer is a lidar-based sensor that is used for cloud-base height detection. The system provides profiles of uncalibrated backscatter up to 15 km agl with a range resolution of 5 m and a time resolution of 15 s. From these profiles, up to three cloud-base heights were determined based on a threshold method of the Lufft algorithm. Ceilometer intercomparisons by Martucci et al. (2010) and Milroy et al. (2012) provide an accuracy of cloud-height detection of about 150 m. We used only the lowest cloud height.

## 2.3 | Near-surface meteorological and air-quality observations

Data of meteorological parameters and air pollutants were available from DWD, from the urban climate stations operated by the Department of Urban Climatology of Stuttgart (City of Stuttgart), and from an operational analytical quality assurance network operated by the State Office for the Environment, Measurements and Nature Conservation of the Federal State of Baden-Württemberg (LUBW).

Mean values of concentrations of $NO_2$, NO, and $O_3$ for every hour were available at the two LUBW stations: AKP (an urban station close to a major road) and BC (an urban background station) (Figure 1, Table 1). $NO_2$ and NO were measured using a $NO_x$ monitor (APNA-370; HORIBA). The reproducibility of measurement was 1% of the full scale. The certified ranges are 0–1200 μg $m^{-3}$ for NO and 0–500 μg $m^{-3}$ for $NO_2$. The $O_3$ measurement was performed using an 49i-PS analyser (Thermo Scientific). The precision of $O_3$ measurement was 2 μg $m^{-3}$. Observations of temperature, air pressure, relative humidity, wind speed, and wind direction were taken from four stations: CZ (City of Stuttgart), BC (LUBW), SB (DWD), and AP (DWD). The AP station is located about 9 km to the southsouthwest of the city of Stuttgart on the Filder plateau (Figure 1), and because of its location at higher elevation outside the Neckar valley, it is assumed to reflect the ambient wind, that is, synoptic or large-scale wind, which is not locally influenced by the slopes and valleys. Mean values of the meteorological parameters for every 10 min were available from stations operated by DWD and the City of Stuttgart and those for every 30 min came from LUBW stations.

## 2.4 | Data availability

In order to study air pollutant concentrations under various nocturnal atmospheric conditions in different seasons of the year, a statistical analysis was performed over the winter and summer period, respectively. In addition, four detailed analyses of 24-h periods, when different cloudiness and winds prevailed, were conducted. Since radiosonde measurements were available only as vertical profiles throughout the entire winter and summer periods (56 soundings for winter and 78 soundings for summer without rain), the soundings were used for the statistics to describe the conditions at midnight. An averaging period of 1 h (from 23:00 to 00:00 UTC) was used for the calculation of parameters from remote sensing data and air pollutant concentrations. One-hour means of these parameters were chosen because their dependence on the radiosonde-based atmospheric stratification on average decreases with increasing averaging intervals. In other words, the representativity of the radio soundings turns out to be best for 1-h periods. The date assignment of the individual cases is at the end of the averaging period, that is, at 00:00 UTC on the following day. $NO_2$ and NO concentrations were available in winter and summer from BC and AKP stations, while $O_3$ values from AKP were available only in winter 2017. The different instruments used in this study are summarized in Table 2.

# 3 | ANALYSIS METHODS AND DATA PROCESSING

In order to analyse the different nights with respect to meteorology and air pollutants, we applied two different approaches characterizing the meteorological conditions: atmospheric stratification, as well as cloudiness and wind conditions. The parameters used to describe both approaches are introduced in the following.

## 3.1 | Stability regimes

As a measure of atmospheric stratification and to determine whether turbulence can exist in the ABL, we used

**TABLE 2** Number of cases used for the nocturnal 1-h period analysis from the different instruments and applied parameters (T is temperature, p is air pressure, $|v|$ is wind speed, and wd is wind direction)

| Device | Used parameter | Number of cases | |
|---|---|---|---|
| | | Winter | Summer |
| Radiosonde (00:00 UTC) | T, p, $\|v\|$, wd | 56 | 78 |
| Ceilometer | Cloud classification | 56 | 78 |
| MWR | T | 46 | 78 |
| Wind lidar in DBS mode | TKE | 21 | 59 |
| Wind lidar in 'vertical stare mode' | $\sigma_w$ | 23 | 15 |
| Meteorological surface stations AP, BC, SB and SZ | T, $\|v\|$, wd | 56 | 78 |
| Air pollutant stations AKP and BC | NO, $NO_2$, $O_3$ | 56 (49) | 78 (45) |

*Note*: The number of cases for all devices is given after quality control. The number of $NO_2$, NO, and $O_3$ data used for the 24-h period (Figure 6) is given in brackets.

the bulk Richardson number (Rib), which is the dimensionless ratio of buoyant generation or suppression of turbulence to shear generation of turbulence. We apply the formula according to Stull (1988) for two discrete height levels. The vertical gradients of the horizontal wind speed ($\frac{\Delta v}{\Delta z}$) and potential temperature ($\frac{\Delta \Theta}{\Delta z}$) between two levels were calculated for the lowest 200 m agl of the radiosonde data. The upper level of Rib calculation at 200 m agl (566 m asl) lies about 40 m above the mean ridge height. This means the layer mostly characterizes the stratification of the valley atmosphere. For the lower level of potential temperature, we used the mean value between 0 and 20 m agl to minimize local effects. Wind speed at the lower level was taken as zero.

In order to determine the different stability regimes, the Rib value has to be compared with a critical Richardson number, Ribc (Stull, 1988). To cover the possible range of atmospheric stratification (see Appendix A), we apply two Ribc values, 0.33 and 1.25, to characterize the investigated nocturnal conditions and assume that dynamically stable flows exist for Rib >1.25 (denoted as the RIBC1 regime) and dynamically unstable flows exist for Rib <0.33 (denoted as RIBC3 regime). The stability regime in between, that is, 0.33 < Rib < 1.25 (denoted as RIBC2 regime), is either dynamically stable or unstable.

### 3.2 | Cloud layers, ambient wind, and nocturnal low-level jet

The presence of clouds and their height in the atmosphere impact the radiative cooling at the surface and thereby the stability of the NBL. We divided the investigated nocturnal conditions into three different categories with respect to cloudiness: (i) clear sky, (ii) cloudy nights with low clouds (<2 km), (iii) no low clouds but middle-high clouds (2–6 km) or high clouds (7–14 km). The mean cloud-base heights from the ceilometer measurements were determined for the period between 23:00 and 00:00 UTC. For the selection of one of the defined cloud conditions, a respective percentage occurrence of 75% had to be present during that time interval.

Additionally, two categories with respect to wind were separated: strong synoptically driven wind and an LLJ. Both might trigger night-time turbulence due to wind shear. Such turbulence, often intermittent, can affect the vertical structure of the NBL and vertical distribution of air pollutants. Following Bonner (1968) and Stull (1988), we defined LLJ nights when a low-level wind speed maximum exists that is at least 2 m $s^{-1}$ stronger than at the layers above and below while decreasing monotonically towards the surface. Nights with an LLJ are classified as a separate wind category. The definition and identification of strong wind cases and distinction between moderate and strong wind speed are explained in Appendix B.

### 3.3 | Turbulence parameters

The wind lidar data were used to calculate turbulence parameters such as the variance of the vertical wind speed $\sigma_w^2$ and the turbulent kinetic energy TKE. The $\sigma_w^2$ values were computed for 1-h intervals from 7-s observations in the vertical stare mode. The advantage of having a vertically pointed beam position to measure $\sigma_w^2$ has been pointed out by Newman et al. (2016). To ensure good data quality of the variances, a two-step procedure was applied: values with a carrier-to-noise ratio (CNR) lower than −27 dB were discarded, and range gates with data availability of more than 75% within 1 h only were considered. Second, random uncorrelated noise (Lenschow & Kristensen, 1985) was estimated by extrapolating the autocorrelation function to the zero lag (Lenschow et al., 2000) and removed. The first five lags were used to apply a linear fit to the autocorrelation function. The difference between the autocorrelation function at the lag zero and the fit function at the lag zero provides the uncorrelated noise. Note that for winter and summer periods, the uncorrelated noise could reach up to 50% of $\sigma_w^2$, as turbulence during the night is usually small to moderate only (<0.25 $m^2$ $s^{-2}$).

The TKE values allow the characterization of buoyancy and/or shear-driven turbulence. TKE is calculated from the velocity variances $\sigma^2$ of the wind components $u$, $v$, and $w$ (e.g., Stull, 1988). We calculated TKE from the wind lidar data in DBS mode and for 1-h intervals based on the 10-min $\sigma_u$, $\sigma_v$, and $\sigma_w$ values provided by the Leosphere software. The values were filtered by using a 10-min-averaged CNR threshold and removing values lower than −21 dB. Finally, range gates with an availability of more than 75% within each 1-h interval only were used. The TKE and $\sigma_w^2$ values, calculated for the period from 23:00 to 00:00 UTC, were then averaged over the lowest 300 m over device for later use in the statistical analysis.

## 4 | METEOROLOGICAL CONDITIONS IN THE NBL

In the following, we investigate the atmospheric stratification and the dependence of Rib on buoyant suppression and shear generation of turbulence (research question 1), the relationship between stratification-related processes and cloudiness and winds (research question 2), the influence of clouds and wind on atmospheric stratification (research question 3), and relations

between Rib and turbulence intensity (TKE and $\sigma_w^2$, research question 4) in the NBL (see Figure 2) for the summer and winter seasons.

## 4.1 | Atmospheric stratification

Figure 3 shows the distribution of night-time Rib values as a function of the potential temperature gradient $\frac{\Delta\theta}{\Delta z}$ (as a proxy for buoyant suppression of turbulence) and squared wind speed gradient $\left(\frac{\Delta v}{\Delta z}\right)^2$ (shear generation of turbulence) for winter and summer. The indicated isolines of Rib = 0.33 and Rib = 1.25 separate the three introduced stability regimes RIBC1, RIBC2, and RIBC3.

In winter (Figure 3a), 57% of all nights fall into RIBC3, 30% into RIBC2, and only 13% are assigned to RIBC1. The nights with very large Rib values are caused by large buoyancy suppression of turbulence and rather low shear generation of turbulence. On the other hand, very small Rib values are caused by small buoyancy suppression and rather high shear generation. The nights indicated with W1 (Rib = 5.15 from RIBC1) and W2 (Rib = 0.09 from RIBC3) are presented in the 24-h case studies in Section 6.1.

In summer, most of the cases fall into the regimes RIBC1 (39%) and RIBC2 (37%) and only 24% into RIBC3 (Figure 3b). Once again, the nights with very large Rib values, such as Rib = 47 during the night indicated with S1, are characterized by large buoyant suppression and low shear generation of turbulence. And, as strong shear is mostly absent in summer nights, there are fewer nights with rather low Rib values compared to the winter season. That means, the nights in winter and summer are considerably different with respect to the occurrence of states of atmospheric stratification and the associated processes that are responsible for them.

## 4.2 | Cloudiness and winds

To identify the wind and cloud conditions associated with Rib, the different categories introduced in Section 3.2 (low clouds, middle-high clouds, clear sky, LLJ, moderate or strong wind speed) are also marked in Figure 3.

In winter, in regime RIBC3, low-level clouds (75%) were present during most of the nights (Figure 3a). In regime RIBC2, all types of clouds occurred, while in RIBC1, four out of seven (57%) were clear-sky cases. From the perspective of cloud types, low clouds (green

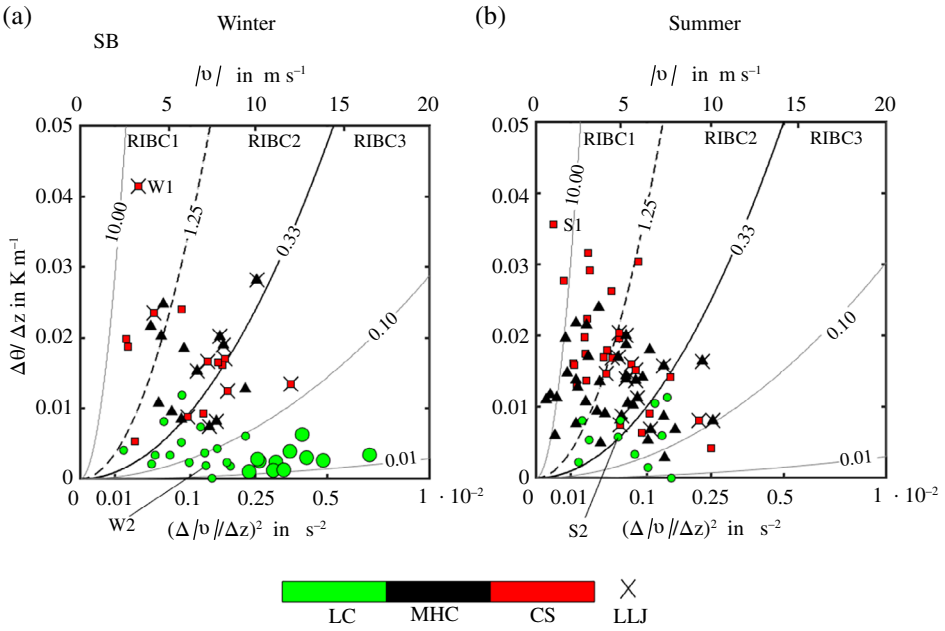


FIGURE 3 Distribution of the Rib values for midnight conditions as a function of the vertical gradient of the potential temperature (as a proxy for buoyant suppression of turbulence), squared gradient of the wind speed (shear generation of turbulence), and wind speed, respectively. Note that the scaling of shear generation is not linear. Both gradients are calculated between 200 m agl and the surface at Schnarrenberg (SB). Symbols: Low clouds (LC, small circles for moderate wind speed, LC1, big circles for strong wind speed, LC2), middle-high clouds (MHC, black triangles), clear skies (CS, red squares), LLJ events (crosses). Rib isolines are in grey. Black isolines of Rib = 0.33 (solid) and Rib = 1.25 (dashed) separate the three stability regimes RIBC1, RIBC2 and RIBC3. $\Theta_{v0}$ used for rib-isoline calculation for winter and summer are means for the corresponding season. W1, W2 and S1, S2 indicate the case study days discussed in Section 6

circles) are all accompanied by small temperature gradients (<0.015 K $m^{-1}$), likely due to low radiative cooling, and a wide range of wind speeds from about 2 to 17 m $s^{-1}$. LLJs (crosses) occurred during 22% of all nights, particularly during nights with middle-high clouds or clear skies (45%). The nights with LLJ events are mainly attributed to RIBC2. The large range of wind speeds during nights with low clouds is also accompanied by a large range of Rib values (Figure 3a). This suggests grouping them separately, that is, into low clouds with moderate wind speed (LC1) and with strong wind speed (LC2, the criterion for separation is given in Appendix B), in order to investigate whether the new categories are also accompanied by different meteorological characteristics and air pollutant concentrations. The LC2 cases are indicated in Figure 3a separately. The corresponding mean Rib value for the LC2 cases is 0.03 ± 0.01, which is considerably lower than that of the LC1 cases (Rib = 0.23 ± 0.24). However, both values are still assigned to the RIBC3 regime.

To get some insight into the vertical structure of the lower troposphere, vertical profiles of mean wind speed and potential temperature gradients calculated for the defined cloudiness and wind categories (nights with low clouds [LC1, LC2], middle-high clouds, clear skies, and LLJ events) are displayed in Figure 4. LC2s and LLJs show larger wind shear in the lowest 200 m agl than LC1, middle-high clouds, and clear skies (Figure 4a). With respect to mean potential temperature gradients, cloudiness and winds are arranged differently: while the gradients of LC1 and LC2 cases are small in the lowest 200 m agl (<0.005 K $m^{-1}$), that is, the NBL is nearly neutrally stratified, the gradients during nights with middle-high, clear skies, or LLJ events all differ significantly, reaching up to about 0.025 K $m^{-1}$ close to the ground (Figure 4b). The statistical significance of the differences of means here and in the following is based on *t*-tests. Thus, the very low Rib values of the LC2 cases can be assigned to shear-driven turbulence due to high could be mainly traced back to a well-mixed sub-cloud layer only. Well-mixed sub-cloud layers often establish due to radiative cooling at the cloud tops (e.g., Lohou et al., 2020; Moeng, 1986) as well as low negative net radiation at the surface (Kalthoff et al., 2018). These processes prevent the formation of a surface inversion and reduce the suppression of turbulence. The low negative net radiation at the surface is due to the temperature difference between the cloud base and Earth's surface, which in general is quite low. In contrast, strong buoyant suppression of turbulence due to strong negative net radiation at the surface characterizes the atmospheric stratification of NBLs under middle-high cloud and clear sky conditions.

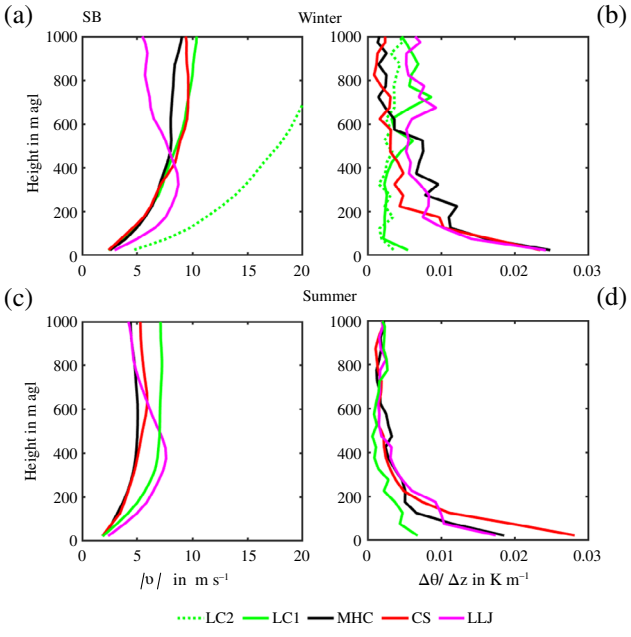


**FIGURE 4** Vertical profiles of mean wind speed (a, c) and mean gradients of potential vertical temperature (b, d) at Schnarrenberg (SB) for different cloudiness and wind conditions (low clouds with moderate wind (LC1), respectively strong wind (LC2), middle-high clouds (MHC), clear skies (CS) and low-level jets (LLJ)). The location of SB is indicated in Figure 1

In summer (Figure 3b), in RIBC3, low clouds occurred in 33%, middle-high clouds in 34%, and clear skies in 28% of all cases. In RIBC1, middle-high clouds and clear skies clearly dominate and amount to 97%. This can be explained by the synoptic conditions governing RIBC1, that is, anticyclones with large-scale subsidence associated with low wind speed and high clouds or clear skies likely result in the formation of a strong surface inversion. Consequently, nights with clear skies are accompanied by temperature gradients reaching up to about 0.035 K $m^{-1}$, as valid for S1, while low clouds prevent the build-up of a strong surface inversion so that the near-surface temperature gradients are <0.01 K $m^{-1}$. LLJ events occurred during 22% of all nights and during 26% of the nights with middle-high clouds or clear skies. As in winter, LLJ cases mainly belong to the regime RIBC2. In contrast to the winter season, the highest wind speeds are connected with LLJ events. The large range of stability regimes during which LLJs exist suggests that different processes are responsible for the generation of the LLJs, for example, inertial oscillation for stably stratified flows but more synoptically influenced for less stably stratified flows (e.g., Stull, 1988).

In summer, three typical mean wind speed profiles can be distinguished (Figure 4c). While the mean wind speeds for middle-high clouds and clear skies are similar

and low (<5.5 m $s^{-1}$ at 1000 m agl), the wind speed values for low clouds and LLJ events are higher. The supergeostrophic wind maximum of the LLJ reaches a value of 7 m $s^{-1}$ at 400 m agl (766 m asl). As expected, clear skies show the greatest mean potential temperature gradient (up to 0.03 K $m^{-1}$ close to the ground) and differs significantly from that of low clouds (<0.008 K $m^{-1}$), that is, a nearly neutral stratification (Figure 4d).

To find out whether the different wind and cloud conditions were accompanied by specific wind directions, wind roses were generated (not shown). The data from 23:00 to 00:00 UTC of the valley stations SB, BC, CZ, and the Filder plateau station AP—the latter assumed to represent the ambient wind—were considered. For the cases with middle-high clouds or clear skies, valley winds prevailed at SB, BC, and CZ both in summer and winter, that is, a southeasterly downvalley flow dominated in the northwest–southeast-oriented Neckar valley and a southwesterly downvalley flow dominated in the Stuttgart basin. Especially during the LC2 cases, often southwesterly ambient winds existed. For these cases, as Rib is low (Figure 3a), coupling between the upper-level ambient wind and the near-surface wind is common. The relationship between ambient winds and valley winds has been investigated in detail by Adler et al. (2020) and Wittkamp et al. (2021).

We also analysed the wind directions during LLJ events in summer and winter by comparing the wind direction at 1 km agl, the mean jet core level (350 m agl), and the near-surface winds at the valley stations. Wind directions at the jet core and 1 km agl were similar and equally distributed without having a preferred wind direction, while the near-surface wind direction depended on the stability regime, that is, on whether coupling existed or not. This means that the wind direction of the LLJ was determined by the ambient wind direction and not related to the topography. Typical examples with the described flow conditions are described in Section 6.

## 4.3 | Relationship between turbulence and atmospheric stratification

The relationships between the turbulence parameters TKE and $\sigma_w^2$ and Rib and the cloudiness and winds are presented in Figure 5. As the wind lidar was either operated in DBS or stare mode, after quality control, the amount of data available for this analysis is reduced (Table 2). On average, the TKE and $\sigma_w^2$ values show a decrease with increasing dynamic stability. Considering both seasons, the exponential regressions for TKE and $\sigma_w^2$ as functions of Rib applied to the RIBC2 and RIBC3 regimes resulted in coefficients of determination of $r^2(\text{TKE}) = 0.43$ and $r^2(\sigma_w^2) = 0.65$. With respect to estimating an Rib threshold for turbulence (Ribc), a value of 0.33 seems to be more appropriate than 1.25 (see discussion in Appendix A) and fits with the results of Banta et al. (2003) which are also based on Rib and TKE data. For TKE and $\sigma_w^2$, all regression coefficients and means are included in Table 3. Although standard deviations and regression coefficients indicate a rather poor relationship, we think that it is worth presenting them, as direct measurements of turbulence in the urban NBL based on wind lidar data are rare.

During LLJ events, the variability of TKE and $\sigma_w^2$ is quite large (Figure 5). The strength of the observed LLJs

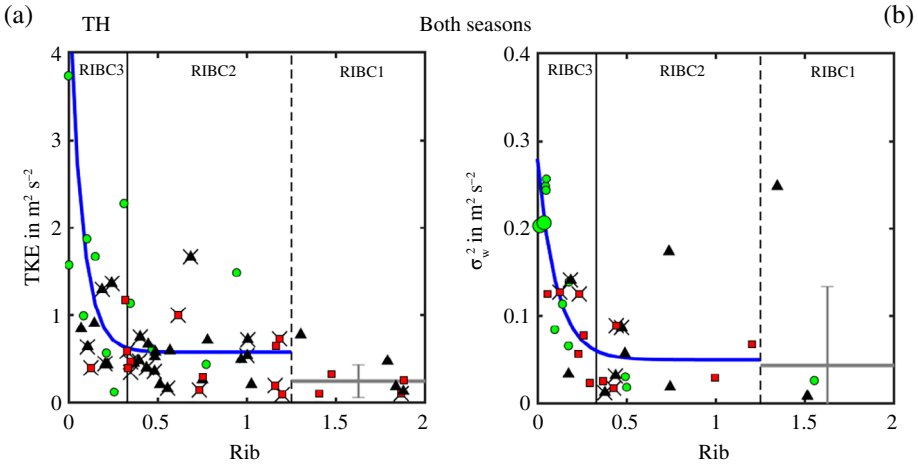


FIGURE 5 TKE (a) and $\sigma_w^2$ (b) using data from both seasons as a function of Rib (note values with Rib >2 are not plotted). Symbols: Low clouds (LC1, small circles; LC2, big circles), middle-high clouds (MHC, triangles), clear skies (CS, squares), LLJ events (crosses). Rib = 0.33 (solid) and Rib = 1.25 (dashed) separate the three stability regimes RIBC1, RIBC2, and RICB3. TKE and $\sigma_w^2$ are measured at TH, Rib calculated from the radio soundings at SB. The positions of the different stations are indicated in Figure 1. Regression line for sectors RIBC3 and RIBC2 (blue), mean value, and standard deviation of variables for the sector RIBC1 (grey). The statistics of the regression and means are given in Table 3

| | Winter | Summer |
|---|---|---|
| $NO_x$ (BC) in µg $m^{-3}$ | $NO_x = 89 \times Rib + 16$<br>$r^2 = 0.40$<br>$NO_x = 108 \pm 21$ | $NO_x = 91 \times Rib + 62$<br>$r^2 = 0.58$<br>$NO_x = 34 \pm 10$ |
| $NO_x$ (AKP) in µg $m^{-3}$ | $NO_x = 87 \times Rib + 65$<br>$r^2 = 0.24$<br>$NO_x = 189 \pm 59$ | $NO_x = 20 \times Rib + 33$<br>$r^2 = 0.14$<br>$NO_x = 51 \pm 17$ |
| $\sigma_w^2$ (TH) in $m^2$ $s^{-2}$ | $\sigma_w^2 = a \times e^{-b \cdot Rib} + c$<br>$a = 0.25 \pm 0.12$, $b = 6.73 \pm 8.05$, $c = 0.05 \pm 0.07$<br>$r^2 = 0.65$<br>$\sigma_w^2 = 0.04 \pm 0.09$ | |
| TKE (TH) in $m^2$ $s^{-2}$ | $TKE = a \times e^{-b \cdot Rib} + c$<br>$a = 4.27 \pm 1.52$, $b = 13.75 \pm 9.30$, $c = 0.58 \pm 0.40$<br>$r^2 = 0.43$<br>$TKE = 0.25 \pm 0.19$ | |

**TABLE 3** Regression formula, coefficient of determination $r^2$, estimated using data for sectors RIBC2 and RIBC3, and mean value and standard deviation for sector RIBC1 for the different stations (see Figure 1)

*Note*: The formulas for $\sigma_w^2$ and TKE are based on both seasons; for the regression formula for RIBC2 and RIBC3, the coefficients include 95% confidence bounds.

(Figure 4a,c) can be classified as moderate (Banta, 2008). The LLJ cases mostly belong to the RIBC2 regime (Figure 3), which is comparable to what Banta (2008) denotes as the transitional regime between weakly stable and strongly stable stratification. Turbulence in this range is characterized as bursting and intermittent (Corsmeier et al., 1997; Ohya et al., 2008) and by sporadic coupling between the atmosphere and the surface (Karipot et al., 2006), which may explain the large variability in TKE and $\sigma_w^2$. Note, however, that TKE and $\sigma_w^2$ of the wind lidar are also the parameters most prone to measurement uncertainties. The turbulence during night-time is quite low, and uncorrelated noise is high (Section 3.3). That means that part of the weak correlation between Rib and the turbulence parameters might be due to the uncertainty of the turbulence measurements as well.

## 5 | RELATIONSHIP OF AIR POLLUTANTS WITH ATMOSPHERIC STRATIFICATION AND CLOUDINESS AND WINDS

In this section, we deal with research question 5 by investigating how the nocturnal near-surface $NO_x$ and $O_3$ concentrations at different urban sites and different times of the seasons relate to atmospheric stratification.

### 5.1 | Diurnal cycle of $NO_x$ and $O_3$ concentrations for different cloudiness and winds

We first review the mean diurnal time series of $NO_x$ and $O_3$ concentrations for different cloudiness and wind categories before we focus on the relations at night-time in the second part. Time series are presented from the BC station and both seasons (note that there are no $O_3$ data at AKP in summer). Only those days were considered where the selected cloud types occurred for at least 75% of the time during the 24-h period. At the BC site, well-known diurnal cycles of $NO_x$ and $O_3$ concentrations, typical of many cities worldwide (Sanchez et al., 2007), are observed (Figure 6). $NO_x$ exhibits a double wave with a morning and late-afternoon peak, coinciding with the rush-hour traffic. The increase in $O_3$ at daytime correlates with the decrease in $NO_x$ due to photochemical formation and convectional mixing. The decrease in $O_3$ after sunset can presumably be traced back to NO titration and dry deposition. Although these general features are visible during both seasons and for most cloudiness and wind categories, differences are evident, too.

In winter, the morning peak of $NO_x$ concentration on average appears between 07:00 and 08:00 UTC (local time = UTC + 1), while the evening peak appears between 20:00 and 21:00 UTC for all wind and cloud conditions (Figure 6a). The morning peak was higher than the evening peak for all cloudiness and wind categories. This can be attributed to shorter rush hours in the morning (Mayer, 1999) and the quite deep and strong surface inversion still present in the morning in winter. The $NO_x$ concentrations for clear sky, middle-high clouds, and LLJ events are higher than for days with low clouds, especially at night-time; for example, at 00:00 UTC, the concentrations for clear skies, middle-high clouds, and LLJ events are about 3 times higher than those for nights with low clouds of LC1 type and 3.5 times higher than of LC2 type. This is because air pollutants are trapped within the surface inversion that is present under clear skies, middle-high clouds, and LLJ events but stronger mixing under LC1 and LC2 conditions (Figure 4b and Section 5.2). This result confirms the findings of other

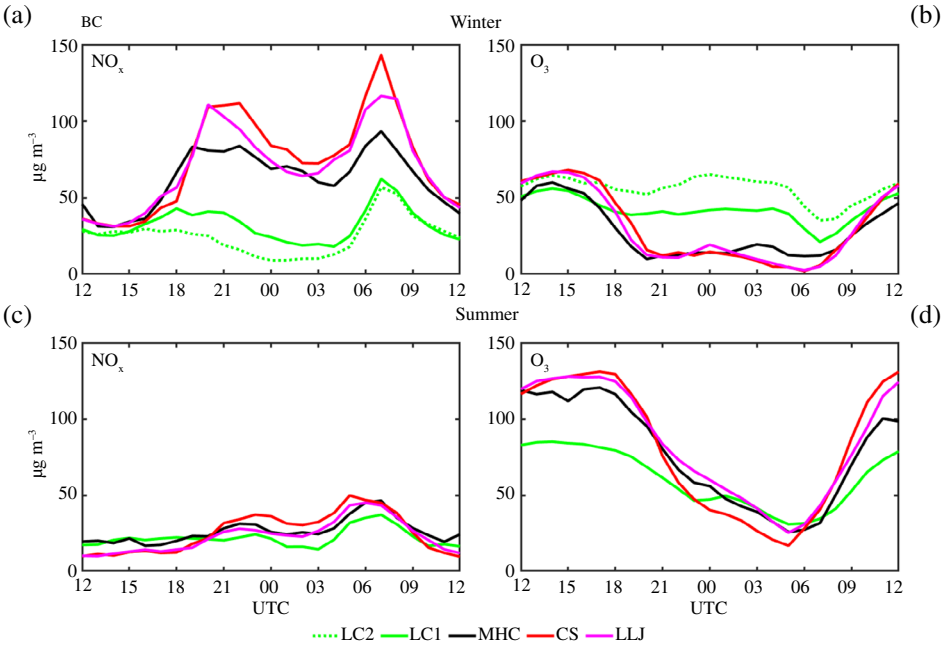


**FIGURE 6** Mean diurnal cycles of hourly averaged $NO_x$ and $O_3$ concentrations at Bad Cannstatt (BC) station for winter and summer for different cloudiness and wind categories (low clouds with moderate wind (LC1) respectively strong wind (LC2), middle-high clouds (MHC), clear skies (CS) and low-level jets (LLJ)). The position of BC is indicated in Figure 1

studies in which wind speed showed a negative correlation with $NO_x$ concentration (Jones et al., 2010; Wang et al., 2020).

In summer, the amplitudes of the diurnal cycle of $NO_x$ for all cloudiness and wind categories are only moderate (<30 μg m$^{-3}$) (Figure 6c). The nocturnal $NO_x$ concentrations, which are highest for clear skies, can be related to the presence of a correspondingly stronger surface inversion than for the other cloudiness and wind categories (Figure 4d and Section 5.2). Because of this, for most of the cloudiness and wind categories, the $NO_x$ concentrations are much lower in summer than in winter, which is due to the lower pollutant emissions and more favourable vertical air mass exchange during daytime in summer. These seasonal differences are also consistent with previous findings (Boersma et al., 2009; Lamsal et al., 2010; Mayer, 1999; Wang et al., 2020). However, while the $NO_x$ concentrations during daytime in summer for all cloudiness and wind categories are about 2.5 times lower than for clear sky, middle-high clouds, and LLJ cases in winter (Figure 6a,c), they are comparable to the $NO_x$ cycles of the low-cloud cases in winter.

In winter, the highest $O_3$ concentrations are noted in the afternoon between 13:00 and 16:00 UTC, while the lowest concentrations occur at night-time (Figure 6b). However, for low clouds, both of the LC1 and LC2 type, the night-time minimum of $O_3$ concentrations are nearly indistinguishable, that is, the $O_3$ values in the night are nearly as high as during daytime. In other words, during night-time, the low-cloud cases are significantly higher than clear sky, middle-high clouds, and LLJ events. This indicates that especially for LC2 cases, $O_3$ was efficiently mixed down from the residual layer to the surface due to shear-generated turbulence, as was also reported by Corsmeier et al. (1997, 2006), Reitebuch et al. (2000), Salmond and McKendry (2002), Mathieu et al. (2005), and Hu et al. (2013).

In summer, the time series of $O_3$ concentrations showed that the peak value was reached between 15:00 and 18:00 UTC (local summertime = UTC + 2) (Figure 6d). During this period, the $O_3$ concentrations are about 2–3 times higher than in winter, except for low clouds, caused by greater solar irradiation and more intense vertical mixing, bringing air with higher $O_3$ concentration down to the surface. In the night, the $O_3$ concentrations for middle-high clouds, low clouds, and LLJ events do not differ much from each other, while for clear skies $O_3$ decreases more strongly in the evening, likely because it is more effectively removed from the atmosphere by dry deposition at the surface or by stronger titration in the more stable NBL.

## 5.2 | Relationship between $NO_x$ concentrations and stability regimes

Figure 7 shows the distribution of nocturnal $NO_x$ concentrations at the BC and AKP sites for the different cloudiness and winds as a function of Rib, potential temperature gradient, squared gradient of wind speed, and wind speed. The influence of the stability regime on $NO_x$ concentrations becomes evident for the winter season at both sites alike (Figure 7a,b). The increase in stability from dynamically unstable to dynamically stable

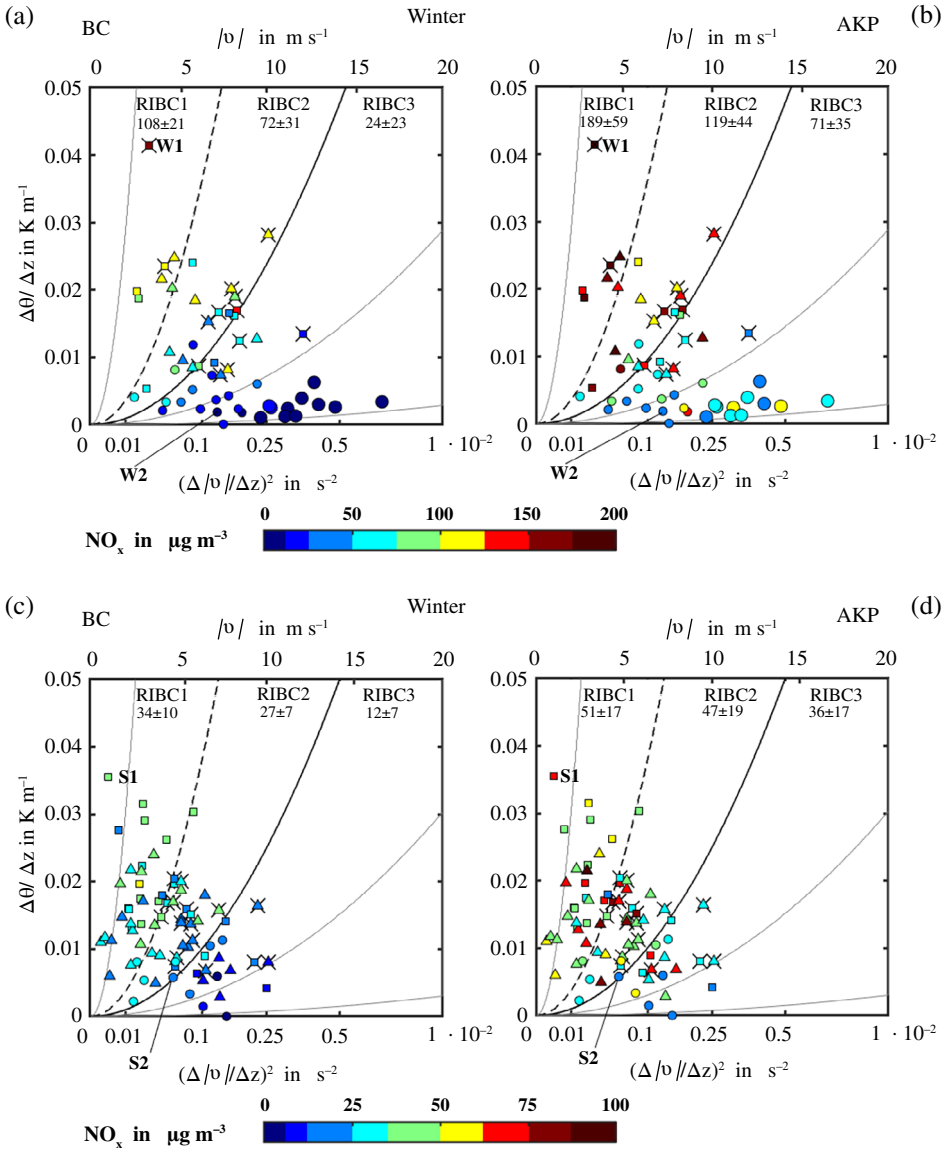


**FIGURE 7** Distribution of Rib and associated $NO_x$ values (colour-coded) at BC and AKP for winter and summer around midnight as a function of the gradient of the potential temperature (as a proxy for buoyant suppression of turbulence), squared gradient of the wind speed (shear generation of turbulence), and wind speed, respectively. Note the scaling of shear generation is not linear. Both gradients are calculated between 200 m agl and the surface. Symbols: Low clouds (LC, small circles for moderate wind speed, LC1, big circles for strong wind speed, LC2), middle-high clouds (MHC, triangles), clear skies (CS, squares), LLJ events (crosses). Rib isolines are in grey. Rib isolines of Rib = 0.33 (solid) and Rib = 1.25 (dashed) separate the three stability regimes RIBC1, RIBC2, and RIBC3. $\Theta_{v0}$ used for Rib-isoline calculation for winter and summer are means for the corresponding season. Numbers indicate mean and standard deviation of $NO_x$ for the corresponding regimes. W1, W2 and S1, S2 indicate the days discussed in Section 6. The positions of BC and AKP are given in Figure 1

flow is accompanied by a significant increase in the mean $NO_x$ concentrations at both sites, that is, at BC from $NO_x(RIBC3) = 24 \pm 23$ to $NO_x(RIBC1) = 108 \pm 21$ µg m$^{-3}$ and at AKP from $NO_x(RIBC3) = 71 \pm 35$ to $NO_x(RIBC1) = 189 \pm 59$ µg m$^{-3}$. This result agrees with those of other studies, which also showed that $NO_x$ concentrations are closely related with stability (Corsmeier et al., 2006; Güsten et al., 1998; Li et al., 2005). It is also found that the concentrations at the BC station (Figure 7a) are much lower than at the AKP site (Figure 7b) for the different stability regimes. While the mean ratio of $NO_x$ concentrations for BC/AKP for the RIBC2 and RIBC1 regimes is approximately 0.5, it amounts to approximately 0.3 for the RIBC3 regime. These values can be explained by the fact that AKP is classified as an urban station close to a road with traffic whereas BC is an urban background station. Additionally, the standard deviation at BC is lower than at AKP. The lowest concentration at the BC station is observed for the LC2 cases (Figure 7a). For example, the mean concentration for LC1 is $NO_x = 33 \pm 29$ µg m$^{-3}$, which differs significantly from the LC2 cases, where $NO_x = 9 \pm 3$ µg m$^{-3}$. At the AKP station, such a significant difference between LC1 and LC2 cases was not observed. The concentration of $NO_x$ is $71 \pm 38$ µg m$^{-3}$ for LC1 cases and $67 \pm 23$ µg m$^{-3}$ for LC2 cases.

Figure 8a shows the relationship between $NO_x$ and Rib for the BC site in winter. The linear correlation is restricted to RIBC2 and RIBC3, and a mean value is determined for RIBC1. All cloudiness and wind categories in winter are considered. The coefficient of determination is poor, mainly because $NO_x$ concentrations during LLJ events seem to be not well correlated with Rib. As discussed in Section 4.3, we assume that most of the LLJ cases, especially the ones

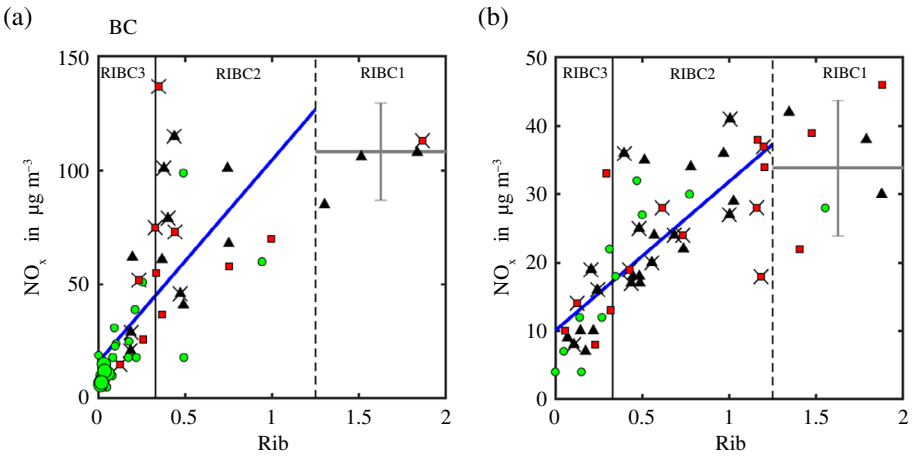


**FIGURE 8** $NO_x$ at BC for winter (a) and summer (b) as a function of Rib (note values with Rib >2 are not plotted). Symbols: Low clouds (LC1, small circles; LC2, big circles), middle-high clouds (MHC, triangles), clear skies (CS, squares), LLJ events (crosses). Rib = 0.33 (solid) and Rib = 1.25 (dashed) separate the three stability regimes RIBC1, RIBC2, and RICB3. Rib calculated from the radio sounding at SB and $NO_x$ measurements are from BC. The positions of the different stations are indicated in Figure 1. Regression line for sectors RIBC3 and RIBC2 (blue), mean value, and standard deviation of variables for the sector RIBC1 (grey). The statistics of the regression and means are given in Table 3

associated with Rib values around 0.33, are related to bursting or intermittent turbulence so that vertical exchange of air pollutants between the surface and the atmosphere is sporadic (Corsmeier et al., 1997; Karipot et al., 2006; Ohya et al., 2008) and hard to describe by bulk numbers such as Rib.

In summer, the influence of atmospheric stratification on the nocturnal $NO_x$ concentrations at both sites is evident, too, although the absolute values are much lower (Figure 7c,d). $NO_x$ concentrations for the RIBC1 and RIBC2 regimes reach up to only about 30% compared to those in winter, and for RIBC3 up to about 50% (Figure 7a,b and c,d). The coefficient of determination for BC is $r^2 = 0.58$ (Figure 8b), while it is considerably poorer for AKP (Table 3), which indicates that additional factors such as advection and thermally driven circulations influence the nocturnal air pollutant concentrations in the urban environment. All four relations and all regression coefficients in each relation are significant at the 5% significance level. The statistical significance of each regression was tested using the *F*-test and the significance of the regression coefficients using the *t*-test.

## 6 | CASE STUDIES FOR DIFFERENT STABILITY REGIMES, CLOUDINESS, AND WINDS

The results shown in Section 5 are based on stability regimes valid for a restricted nocturnal period (23:00–00:00 UTC) and not necessarily representative for the entire night. As mentioned, the variability of air pollutant concentrations within the individual cloudiness and wind categories or stability regimes could be high. Therefore, in the following, we present four working days, two for each season: days with dynamically stable (RIBC1, winter, W1; summer, S1); a case assigned to the transition from dynamically stable to unstable (RIBC2-RIBC3, summer, S2); and an unstable (RIBC3, winter, W2) flow during the night (the individual nights are labelled in Figures 3 and 7). Figure 9 shows the profiles of the potential temperature and gradient of potential temperature of the nocturnal radio soundings for the four cases. Using a threshold of 0.005 K $m^{-1}$ for the detection of the depth of the stable NBL, the two dynamically stable cases, W1 and S1, are characterized by strong surface inversions strengths and shallow NBL depths of about 615 m asl (250 m agl), while the transition case, S2, is characterized by a weak surface inversion strength but deeper NBL of 715 m asl (350 m agl). The dynamically unstable case, W2, is not associated with a surface inversion at all.

Before we start with the detailed analysis, we contrast the four cases by comparing wind direction measurements at surface stations at different altitudes with the wind direction at 700 m asl measured by the nocturnal radio sounding (Figure 10). Clear differences are visible for the individual nights. During the dynamically stable flows (W1 and S1), wind direction differed at the individual heights, indicating a nocturnal decoupling between the atmosphere and the surface: at CZ in the Stuttgart basin and at BC in the Neckar valley, southwesterly and southeasterly downvalley wind was present. At AP on the Filder plateau and in the radio sounding, the wind revealed a northerly component. During the dynamically

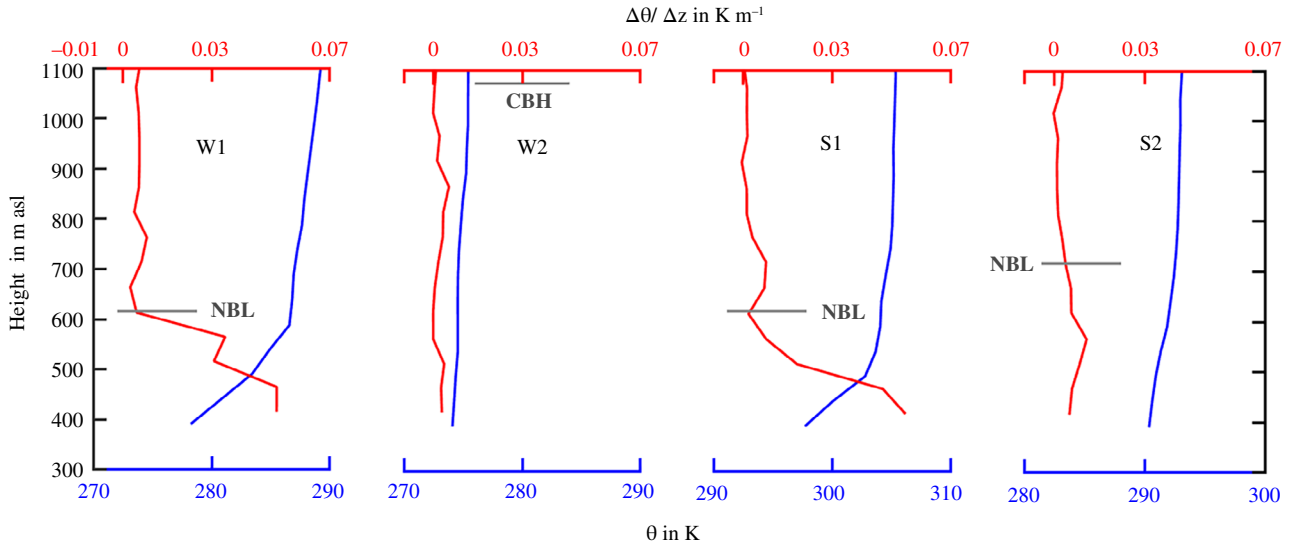


FIGURE 9 Vertical profiles of potential temperature (blue) and of gradients of potential temperature (red) from the night-time radio soundings (22:45 UTC) at Schnarrenberg (SB) during winter cases W1, W2 and summer cases S1, S2. In W1, S1, and S2, NBL indicates the top of the stable nocturnal boundary layer. In W2, CBH indicates the cloud base height derived from ceilometer measurements at SB. The positions of the stations are given in Figure 1

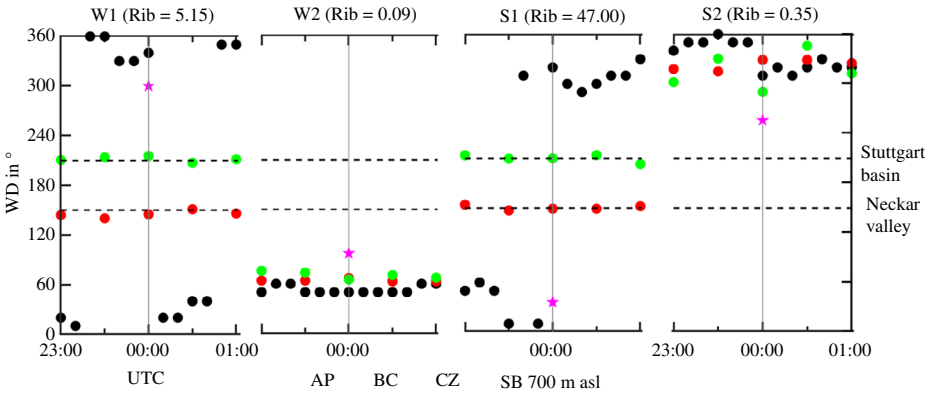


FIGURE 10 Wind directions during cases W1 and S1 (dynamically stable flow in winter and summer, respectively) and during cases W2 and S2 (dynamically unstable flow in winter and summer, respectively). Shown are near-surface wind direction, WD, at City Centre (CZ, 300 m asl) in the Stuttgart basin, at Bad Cannstatt (BC, 303 m asl) in the Neckar valley, and at Stuttgart airport (AP, 411 m asl) on the Filder plateau, as well as the 23:00 UTC wind direction of the radio sounding from Schnarrenberg (SB) at 350 m agl (≈700 m asl). The dashed lines indicate the orientation of the Stuttgart basin respectively Neckar valley for down-valley winds. Positions of the different stations are given in Figure 1

unstable flow (W2) and transition flow case (S2), the wind direction was similar at the individual heights with northeasterly flow during W2 and northwesterly flow during S2, indicating a nocturnal coupling between the atmosphere aloft and the surface.

## 6.1 | The winter cases of 10 and 16 February 2017

A clear-sky case with an LLJ and representative of the RIBC1 regime was 16 February (indicated by W1 in Figures 3a and 7a,b). The synoptic situation was dominated by a high-pressure system leading to cloud-free conditions during the 24-h period from 06:00 UTC on 15 February to 06:00 UTC on 16 February (Figure 11g). In the morning of 15 February, a deep surface inversion with an inversion strength of 0.03 K $m^{-1}$ near the surface existed (Figures 3a and 11c). Around 600 m asl, a weak nocturnal LLJ from southwest with wind speeds of 5 m $s^{-1}$ at the jet core was detected (Figure 11a). After 07:00 UTC, the transition from a stable to a neutrally stratified, well-mixed layer, accompanied by a continuous increase in TKE (Figure 11c), took place. By about 10:00

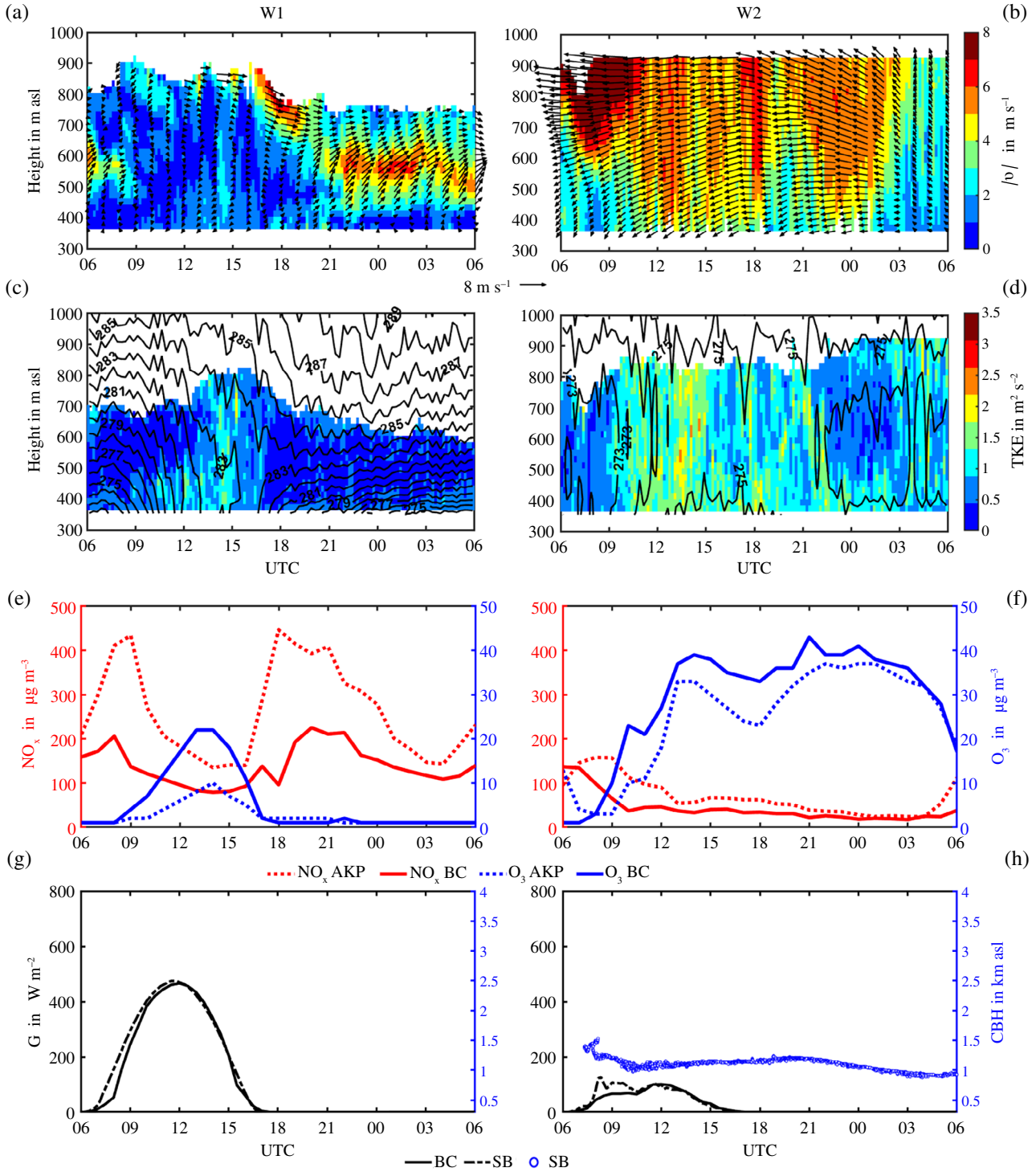


**FIGURE 11** Time–height diagrams of horizontal wind speed (colour-coded) and wind direction (wind vectors) (a,b), of potential temperature (black isolines) and TKE (colour-coded) (c,d) based on wind lidar and microwave radiometer observations at TH, time series of near-surface $NO_x$ (red lines), and $O_3$ concentrations (blue lines) (e,f), solar irradiation, G, (black lines) (g) and cloud-base height (blue circles) (h) for W1 (16 February) and W2 (10 February). For the positions of the different measurement stations, we refer to Figure 1

UTC, TKE values in the lowest 450 m asl reached up to 1–1.5 $m^2\ s^{-2}$ and the wind had slightly increased to 3 $m\ s^{-1}$ blowing from a northeasterly direction. Around noontime, the near-neutral stratified layer reached its maximum height of 500 m asl. After 17:00 UTC, a surface inversion started to form, resulting in a strongly stable and shallow NBL at both sites (TH and SB) around midnight, as indicated by the microwave radiometer and

radio sonde observations, respectively (Figures 9 and 11c). Parallel to the evolution of the surface inversion, an LLJ formed during the night, with a wind speed maximum of 8 m $s^{-1}$ at the jet core at 550 m asl (Figure 11a). Despite the LLJ and the associated shear, no enhanced turbulent mixing was observed, and TKE values stayed below 1.0 $m^2$ $s^{-2}$ at all heights (Figure 11c).

The corresponding diurnal cycles of $NO_x$ and $O_3$ concentrations at AKP and BC are shown in Figure 11e. The temporal evolution during W1 was typical of clear-sky cases (Figure 6a,b). The morning and evening peaks of the $NO_x$ concentrations were associated with the emission and accumulation of air pollutants in the surface inversion layer. At AKP, the concentrations reached a maximum value of 450 μg $m^{-3}$ and at BC up to 200 μg $m^{-3}$. $O_3$ at these times exhibited low values due to titration by abundant NO and dry deposition. As typical of nocturnal pollutant concentrations under dynamically stable flows (Figure 6a,b), the $NO_x$ concentrations at the AKP and BC remained high (100 μg $m^{-3}$ at BC and 150 μg $m^{-3}$ and AKP) (Figure 11e) due to missing of shear-generated turbulent mixing (Figure 11c), so that air pollutants were trapped in the shallow NBL.

The case of 10 February is representative of the RIBC3 regime and was characterized by low clouds and weak winds (LC1, W2 in Figures 3a and 7a,b). During nearly the whole 24-h period from 06:00 UTC on 09 February to 06:00 UTC on 10 February, the sky was overcast by low clouds with a cloud-base height of about 850–1350 m asl (Figure 11h). Neither in the morning of 09 February nor in the night of 10 February (Figure 9) did distinct surface inversions develop due to absence of radiative cooling of the Earth's surface. Instead, the sub-cloud layer was nearly well mixed during the entire period (Figure 11d). Easterly winds prevailed, reaching up to 10 m $s^{-1}$ above 600 m asl on 09 February between 06:00 and 10:00 UTC (Figure 11b). However, at this time, at lower levels the wind speed did not exceed 4 m $s^{-1}$ so that moderate vertical wind shear only allowed TKE to reach values of 0.5–1 $m^2$ $s^{-2}$ (Figure 11d). After about 10:00 UTC and until 02:00 UTC of the following night, the strong easterly wind reached further down (Figure 11b), accompanied by an increase in TKE to 2.5 $m^2$ $s^{-2}$ (Figure 11d). TKE remained high until about 16:00 UTC and stayed moderately high at all detectable altitudes with noticeable temporal variations until about 22:00 UTC. Afterwards, high TKE values of up to about 1.5 $m^2$ $s^{-2}$ were mainly restricted to the lowest about 450 m asl, that is, to the layer with strong vertical wind shear. As solar irradiation was quite low and the surface layer was only weakly thermally unstable during the day (Rib[12:00 UTC] = −0.05) and dynamically unstable during the night (Rib[24:00 UTC] = 0.09) (Figure 11h), vertical wind shear can be considered mainly responsible for TKE production.

The strong mechanically induced turbulence during the night also affected the pollutant concentrations. The downward mixing of $O_3$ on 9 February started at 09:00 UTC, resulting in a rapid $O_3$ increase both at the AKP and BC stations so that values between 30 and 40 μg $m^{-3}$ were reached (Figure 11f). In contrast, $NO_x$ was quite low at the AKP and BC stations. After a small morning peak with concentrations of only about 150 μg $m^{-3}$, the concentrations continuously decreased, and the evening peak was even completely missing.

## 6.2 | The summer cases of 23 and 31 August 2018

A clear-sky case (indicated by S1 in Figures 3b and 7c,d) and a representative of the RIBC1 regime was 23 August. In the morning of 22 August, a strong surface inversion was visible favoured by a cloudless sky (Figure 12c,g). At 06:00 UTC, the strength of the surface inversion was about 0.02 K $m^{-1}$. Until 09:00 UTC, easterly winds at all observed heights did not exceed 2 m $s^{-1}$. Caused by increasing solar irradiation (Figure 12g), the stable surface layer was eroded at around 09:00 UTC (Figure 12c). Until 12:00 UTC, the solar irradiation reached 780 W $m^{-2}$, and a 1.65-km deep convective boundary layer (CBL) was established, according to the radio sounding (not shown). The CBL persisted until about 15:00 UTC, associated with moderate winds, and TKE values reached up to 3.5 $m^2$ $s^{-2}$ (Figure 12c). After 12:00 UTC, broken low-level clouds partly reduced the incoming radiation at the surface. At around 15:30 UTC, a convective thunderstorm passed the investigation area, accompanied by strong southwesterly winds of up to 13 m $s^{-1}$, high TKE (1.5–3.5 $m^2$ $s^{-2}$), a short precipitation event of 0.1 mm within 10 min, and a temperature drop in the lowest 600 m asl (Figure 12c). The temperature decrease was probably caused by evaporative cooling of raindrops below the cloud base. After 16:00 UTC, the atmosphere became stably stratified and TKE did not exceed 0.5 $m^2$ $s^{-2}$ for several hours. The period from 17:00 to 22:00 UTC was characterized by low wind and TKE values, the clouds dissolved, and a strong and shallow surface inversion started to form (Figures 9 and 12a, c,g). After 22:00 UTC, however, the westerly winds increased again, reaching up to 3–6 m $s^{-1}$. The wind speed maximum at about 02:30 UTC on 23 August was accompanied by TKE values of 1–2 $m^2$ $s^{-2}$.

Because of the lower emissions and stronger convective vertical mixing in summer than in winter, the $NO_x$ concentrations were low on this day (Figure 12e). While at the BC station weak morning and evening peaks were detectable, at the AKP station these two peaks did not

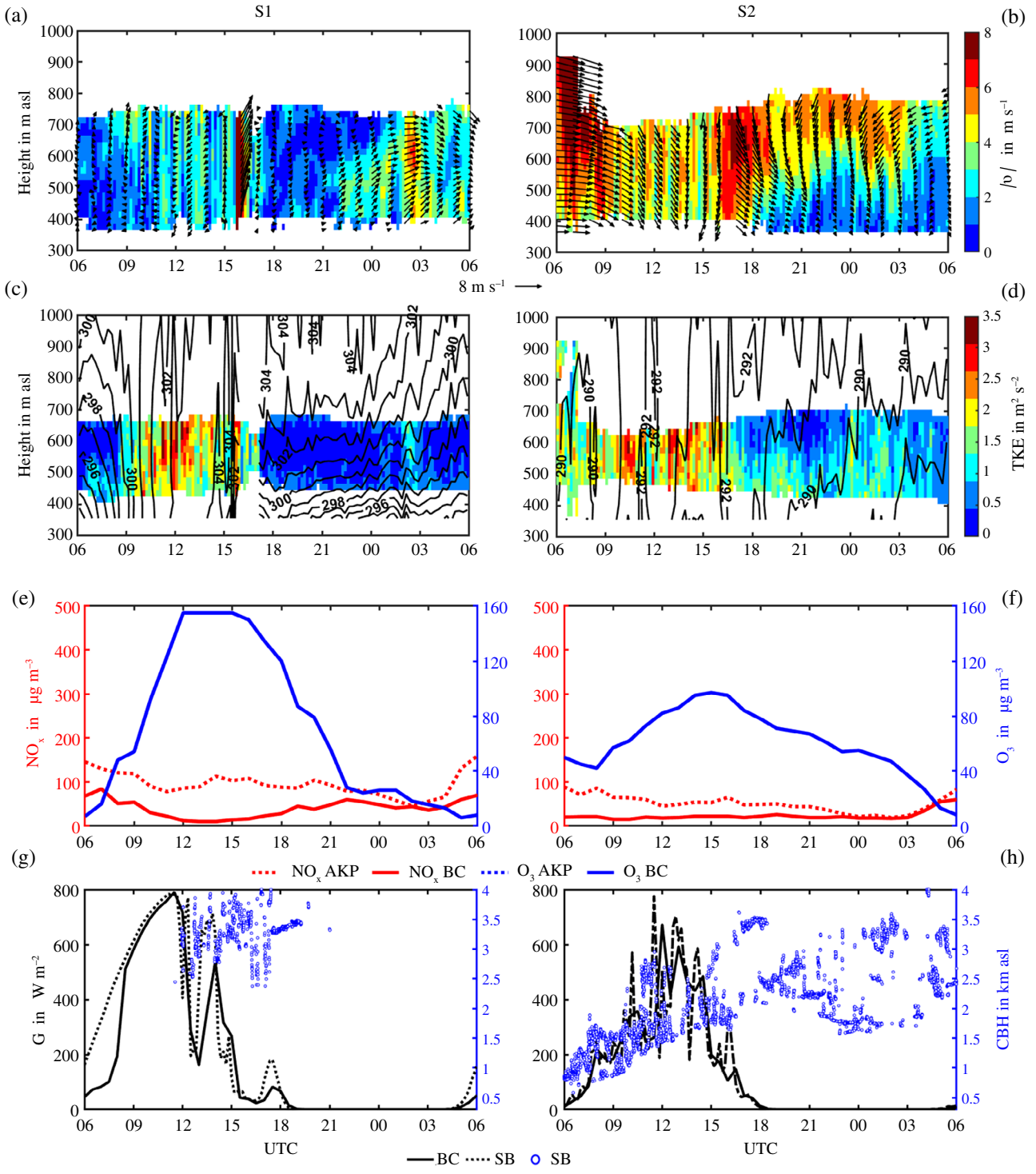


**FIGURE 12** Time–height diagrams of horizontal wind speed (colour-coded) and wind direction (wind vectors) (a,b) of potential temperature (black isolines) and TKE (colour-coded) (c,d) based on wind lidar and microwave radiometer observations at TH, time series of near-surface $NO_x$ (red lines) and $O_3$ concentrations (blue lines) (e,f), solar irradiation, G, (black lines) (g) and cloud-base height (blue circles) (h) for S1 (23 August) and S2 (31 August). For the positions of the different measurement stations, we refer to Figure 1

show up. At BC, strong turbulent mixing even resulted in a reduction of $NO_x$ to <20 µg $m^{-3}$ in the early afternoon. The strong increase in near-surface $O_3$ concentrations in the morning can be explained by photochemical production of $O_3$ and turbulent downward mixing from the residual layer to the ground (Figure 12c,e,g). The decrease in $O_3$ in the afternoon was accompanied by a rapid decrease in solar irradiation and turbulence.

A day with low clouds (Figure 12h), representing a case assigned to the transition from RIBC2 to RIBC3, was

31 August (S2 in Figures 3b and 7c,d). On 30 August, the cloud base rose from about 600 m asl in the morning to 1500 m asl at mid-day. Consequently, radiative cooling at the surface in the night was reduced, preventing a surface inversion to develop (Figure 12d). In the afternoon and the night from 30 to 31 August, scattered low-level clouds and middle and high clouds covered the sky in the investigation area. From 06:00 to 10:00 UTC, westerly to northwesterly winds prevailed at all heights, reaching values of up to 10 m $s^{-1}$ at elevations between 700 and 900 m asl (Figure 12b). Accordingly, TKE amounted to 1–2.5 $m^2$ $s^{-2}$ (Figure 12d). From 10:00 to 16:00 UTC, the winds calmed down slightly, and the broken clouds allowed the solar irradiation to reach maximum values of 780 W $m^{-2}$ around mid-day (Figure 12h). A 1-km deep CBL visible in the radio sounding at noon (not shown) developed during this period, indicated by neutral stratification, and accompanied by large TKE values of up to 3.5 $m^2$ $s^{-2}$ (Figure 12d). TKE can be considered both shear- and buoyancy-generated. After about 18:00 UTC, winds and TKE weakened considerably in the lowest 500 m asl. However, the NBL became only weakly stable, stratified, and relatively deep (e.g., at SB at 22:45 UTC being about 350 m agl; Figure 9) and, owing to vertical wind shear (Figure 12b), the turbulence was relatively strong throughout the night: the values were up to 1.0 $m^2$ $s^{-2}$ at 700 m asl and up to 2.0 $m^2$ $s^{-2}$ between 450 and 550 m asl (Figure 12d).

Concerning the $NO_x$ concentrations, no morning peaks were present at BC and AKP on 30 August (Figure 12f). The values were about 90 μg $m^{-3}$ at AKP and about 20 μg $m^{-3}$ at BC. In the course of the day, $NO_x$ concentrations decreased continuously at AKP and remained at a low level at BC. Evening peaks were missing at both sites. This is consistent with the high wind speed and associated shear-generated turbulence (Figure 12d). The strong turbulence between 06:00 and 09:00 UTC also led to by a higher $O_3$ concentrations (by a factor of about two) compared to the corresponding period on 22 August (Figure 12e,f). However, on 30 August between 09:00 and 12:00 UTC, the $O_3$ concentrations increased much slower and were lower than on 22 August. While turbulent mixing processes did not differ much on both days between 09:00 and 12:00 UTC, the solar irradiation did, that is, on 30 August it was 54% lower than on 22 August (Figure 12g,h). Therefore, we assume that the photochemical formation of $O_3$ was responsible for the higher concentration on the 22 August, although higher background concentrations in the residual layer could have additionally contributed to the increase in $O_3$ concentrations. Afterwards, that is, from 12:00 to 18:00 UTC (sunset), the solar irradiation was very similar on both days and associated with a continuous decrease in the $O_3$ concentrations. We assume that the nocturnal $NO_x$ concentrations, which were slightly lower during S2 compared to S1 (Figure 12e,f), besides being affected by shear-driven turbulent mixing, were also favoured by the deeper and less stable NBL present during S2 compared to S1.

## 7 | SUMMARY AND CONCLUSIONS

Within the framework of the city climate project $[UC]^2$, meteorological and air pollutant measurements were performed in various cities of different topographic complexities in Germany (Scherer, Ament, et al., 2019b). The project aims at improving the understanding of city climates and to investigate the connection between meteorological conditions and air pollutant concentrations. Additionally, such measurements will provide high-quality data for the evaluation of the newly developed large-eddy simulation model PALM-4U (Maronga et al., 2019; Scherer, Florian, et al., 2019a). In this study, we used data from the measurement campaigns conducted in the Stuttgart area during winter 2017 and summer 2018. This city was chosen because it is embedded in a complex orographic environment characterized by a basin-shaped valley (Stuttgart basin) that opens into the larger Neckar valley and is known for its air quality issues.

We concentrated on the state of the NBL and investigated how the atmospheric stratification was related to cloudiness and winds and how the nocturnal near-surface $NO_x$ and $O_3$ concentrations were influenced by these atmospheric conditions (Figure 2). Atmospheric stratification was classified using the bulk Richardson number. Wind information was chosen because, for example, strong synoptic winds or LLJs could cause shear-generated turbulence and by this affect vertical mixing of air pollutants in the NBL. For separation of the stability regimes, two critical Rib values were used, namely 0.33 and 1.25, characterizing the range between dynamically stable and unstable flows using thresholds suggested from previous investigations.

For the investigations, we used data from near-surface meteorological and air pollutant observations as well as vertical profiling data, both in situ and by remote sensing, positioned in the Stuttgart basin, in the adjacent Neckar valley, and on the Filder plateau. Especially, the information from the thermal and dynamic profiling systems, which are normally not available for air pollutant studies, gave additional insight into the processes relevant to the temporal behaviour of the air pollutant concentrations. The main findings addressing the five research questions (sketched in Figure 2) are as follows:

(1) In winter nights, dynamically unstable flows (Rib<0.33, RIBC3 regime) dominate (57%), while dynamically stable flows (Rib>1.25, RIBC1 regime) occur most rarely (13%). In summer nights, the occurrences are more uniformly distributed over the different stability regimes (39% in RIBC1, 37% in RIBC2, 24% in RIBC3). In winter, the most unstable flows are caused by strong shear generation and weak buoyant suppression of turbulence alike. Cases with this kind of strong shear generation of turbulence are not observed in summer. During both seasons, most nights with dynamically stable flows (RIBC1) are caused by strong buoyant suppression and weak shear generation of turbulence.

(2 and 3) The investigation of the relation between the different stability regimes and clouds showed that dynamically stable flows (RIBC1) were mainly associated with middle and high clouds or clear skies—a finding that holds for winter and summer. These conditions, typical for the presence of high-pressure systems, allow considerable net radiative cooling at the surface the build-up of strong surface inversions, and associated buoyant suppression of turbulence. These processes are most effective under clear-sky conditions. Dynamically unstable flows (RIBC3) can often be found under conditions with low clouds (75% in winter and 33% in summer). The NBL and the sub-cloud layer during these nights is also very often near-neutrally stratified. Well-mixed, near-neutrally stratified sub-cloud layers can be explained by radiative cooling at the cloud tops and low net longwave radiation (weak cooling) at the Earth's surface (e.g., Kalthoff et al., 2018; Lohou et al., 2020; Moeng, 1986). Especially in winter, the low clouds are accompanied by strong winds, that is, shear generation of turbulent mixing. The analysis of the wind speed profiles reveals that LLJs formed in about 22% of all nights both in winter and summer. The height of the 7–8 m $s^{-1}$ strong jet, on average, is observed between 165 m (winter) and 245 m (summer) above the mean ridge height of the hills surrounding the Stuttgart basin and the Neckar valley, respectively.

(4) The turbulence parameters $\sigma_w^2$ and TKE show turbulent intensity inversely related to Rib values. The largest values occur under dynamically unstable flows (RIBC3) and the lowest under dynamically stable flows (RIBC1). The turbulence data suggest a threshold—indicating the transition from dynamically unstable flows to dynamically stable flows—close to Ribc = 0.33, although the coefficients of determination of the regression curve are only moderate. By this, the observations support the threshold value of, for example, Wetzel (1982) and Banta (2008) (cf. Appendix A). The LLJ cases being only moderate in strength is mainly due to RIBC2, where turbulence is expected to be sporadic. We assume that the sporadic and intermittent appearance of turbulence is responsible for the great variability of TKE and $\sigma_w$ under LLJ conditions, which is comparable to the findings by Banta (2008). The four selected cases studied in more detail clearly show the relation between turbulence intensity, Rib, and the degree of coupling between the ambient wind and near-surface flows both in the Stuttgart basin and Neckar valley.

(5) Air pollutants in summer and winter differ considerably both with respect to absolute values and diurnal cycles. On average, $NO_x/O_3$ concentrations are higher/lower in winter than in summer. The values are higher at AKP (an urban station close to a road with traffic) than at BC (an urban background station in the Neckar valley). In both seasons and at both stations, the $NO_x$ concentrations are positively correlated with Rib—at least in RIBC2 and RIBC3 at BC. We expect that the strong scatter of $NO_x$ at values of about Rib = 0.33, that is, at the transition from RIBC3 to RIBC2, is due to the intermittent and bursting turbulence leading sporadic exchange of air pollutants between the atmosphere aloft and the surface. This phenomenon has also been described by other investigators (Corsmeier et al., 1997; Karipot et al., 2006; Ohya et al., 2008). As the coefficient of determination was only poor for AKP, additional factors must be more important for the nocturnal $NO_x$ concentration in the city centre. The $NO_x$ values under dynamically stable flows are considerably higher than under dynamically unstable flows (3–4 times at AKP and 2–3 times at BC). This again emphasizes the specific role of the atmospheric stratification on the nocturnal air pollutant concentrations.

With respect to the different cloudiness and wind categories, we found that during nights in winter with low clouds, which are associated with strong winds and near-neutral stratification, the $NO_x$ concentrations are much lower than during nights with middle-high clouds and clear skies. Accordingly, $O_3$ shows the opposite behaviour. A case study of a day that falls into the RIBC3 regime (W2) clearly shows that vertical coupling due to turbulence, which occurs over some hundred meters, was responsible for the reduction of near-surface air pollutant concentrations. In summer, as strong winds do not show up, the differences between the air pollutant concentrations for the different cloudiness and wind categories are less pronounced.

Overall, the data collected during the two seasons give a comprehensive overview of the meteorological conditions and air pollutant concentrations as well as their interrelation. Together with the results of characteristics of the horizontal (Adler et al., 2020) and vertical structures of the wind field in the Stuttgart basin and Neckar valley (Wittkamp et al., 2021), the data will be used for evaluation of the PALM-4U model in the ongoing second project phase of

[UC]$^2$. Especially, the information from the ground-based remote sensing systems (wind lidar, MWR), which are normally not available for air pollutant studies, gave additional insight into the processes relevant to the temporal behaviour of the air pollutant concentrations. Therefore, we are convinced that their application could contribute considerably to operational air quality monitoring and forecasting in Stuttgart and other cities. Future studies on dynamic stability of the nocturnal urban boundary layer could look at impacts of heat emissions from home-heating (in winter) and from heat storage in the urban fabric during daytime (in summer).

## ACKNOWLEDGEMENT

Open Access funding enabled and organized by Projekt DEAL.

## AUTHOR CONTRIBUTIONS

**Olga Kiseleva:** Conceptualization (equal); formal analysis (equal); investigation (equal); methodology (equal); visualization (equal); writing – original draft (equal); writing – review and editing (equal). **Norbert Kalthoff:** Conceptualization (equal); formal analysis (equal); investigation (equal); methodology (equal); writing – original draft (equal); writing – review and editing (equal). **Bianca Adler:** Conceptualization (equal); methodology (equal); writing – original draft (supporting); writing – review and editing (supporting). **Meinolf Kossmann:** Data curation (equal); writing – original draft (supporting); writing – review and editing (supporting). **Andreas Wieser:** Data curation (equal). **Rayk Rinke:** Data curation (equal).

## ORCID

*Olga Kiseleva* https://orcid.org/0000-0002-5684-9789

## REFERENCES

Adler, B., Kalthoff, N. & Kiseleva, O. (2020) Detection of structures in the horizontal wind field over complex terrain using coplanar Doppler lidar scans. *Meteorologische Zeitschrift*, 29, 467–481. https://doi.org/10.1127/metz/2020/1031

Banta, R.M. (2008) Stable-boundary-layer regimes from the perspective of the low-level jet. *Acta Geophysica*, 56, 58–87. https://doi.org/10.2478/s11600-007-0049-8

Banta, R.M., Pichugina, Y.L. & Newsom, R.K. (2003) Relationship between low-level jet properties and turbulence kinetic energy in the nocturnal stable boundary layer. *Journal of Atmospheric Sciences*, 60, 2549–2555. https://doi.org/10.1175/1520-0469(2003)060<2549:RBLJPA>2.0.CO;2

Beyrich, F. & Leps, J.-P. (2012) An operational mixing height data set from routine radiosoundings at Lindenberg. *Meteorologische Zeitschrift*, 21, 337–348. https://doi.org/10.1127/0941-2948/2012/0333

Boersma, K.F., Jacob, D.J. & Trainic, M. (2009) Validation of urban $NO_2$ concentrations and their diurnal and seasonal variations observed from the SCIAMACHY and OMI sensors using in situ surface measurements in Israeli cities. *Atmospheric Chemistry and Physics*, 9, 3867–3879. https://doi.org/10.5194/acp-9-3867-2009

Bonner, W.D. (1968) Climatology of the low-level jet. *Monthly Weather Review*, 96, 833–850. https://doi.org/10.1175/1520-0493(1968)096<0833:COTLLJ>2.0.CO;2

Collaud Coen, M., Praz, C., Haefele, A., Ruffieux, D., Kaufmann, P. & Calpini, B. (2014) Determination and climatology of the planetary boundary layer height above the Swiss plateau by in situ and remote sensing measurements as well as by the COSMO-2 model. *Atmospheric Chemistry and Physics*, 14, 13205–13221. https://doi.org/10.5194/acp-14-13205-2014

Conangla, L., Cuxart, J., Jiménez, M.A., Martínez-Villagrasa, D., Miró, J.R., Tabarelli, D. et al. (2018) Cold-air pool evolution in a wide Pyrenean valley. *International Journal of Climatology*, 38, 2852–2865. https://doi.org/10.1002/joc.5467

Corsmeier, U., Kalthoff, N., Kolle, O., Kotzian, M. & Fiedler, F. (1997) Ozone concentration jump in the stable nocturnal boundary layer during a LLJ-event. *Atmospheric Environment*, 31, 1977–1989. https://doi.org/10.1016/S1352-2310(96)00358-5

Corsmeier, U., Kossmann, M., Kalthoff, N. & Sturman, A. (2006) Temporal evolution of winter smog within a nocturnal boundary layer at Christchurch, New Zealand. *Meteorology and Atmospheric Physics*, 91, 129–148. https://doi.org/10.1007/s00703-005-0111-5

Crewell, S. & Löhnert, U. (2007) Accuracy of boundary layer temperature profiles retrieved with multifrequency multiangle microwave radiometry. *IEEE Transactions on Geoscience and Remote Sensing*, 45, 2195–2201. https://doi.org/10.1109/TGRS.2006.888434

De Wekker, S.F.J. & Kossmann, M. (2015) Convective boundary layer heights over mountainous terrain—a review of concepts. *Frontiers in Earth Science*, 3, 77. https://doi.org/10.3389/feart.2015.00077

De Wekker, S.F., Kossmann, M., Knievel, J.C., Giovannini, L., Gutmann, E.D. & Zardi, D. (2018) Meteorological applications benefiting from an improved understanding of atmospheric exchange processes over mountains. *Atmosphere*, 9, 371. https://doi.org/10.3390/atmos9100371

Doran, J.C., Fast, J.D. & Horel, J. (2002) The VTMX 2000 campaign. *Bulletin of the American Meteorological Society*, 83, 537–554. https://doi.org/10.1175/1520-0477(2002)083<0537:TVC>2.3.CO;2

Fast, J.D. & Zhong, S. (1998) Meteorological factors associated with inhomogeneous ozone concentrations within the Mexico city basin. *Journal of Geophysical Research—Atmospheres*, 103(D15), 18927–18946. https://doi.org/10.1029/98JD01725

Giovannini, L., Ferrero, E., Karl, T., Rotach, M.W., Staquet, C., Trini Castelli, S. et al. (2020) Atmospheric pollutant dispersion over complex terrain: challenges and needs for improving air quality measurements and modeling. *Atmosphere*, 11, 646. https://doi.org/10.3390/atmos11060646

Glaser, K., Vogt, U., Baumbach, G., Volz-Thomas, A. & Geiss, H. (2003) Vertical profiles of $O_3$, $NO_2$, $NO_x$, VOC, and meteorological parameters during the Berlin Ozone Experiment (BERLIOZ) campaign. *Journal of Geophysical Research—Atmospheres*, 108(D4), 8253. https://doi.org/10.1029/2002JD002475

Güsten, H., Heinrich, G. & Sprung, D. (1998) Nocturnal depletion of ozone in the Upper Rhine Valley. *Atmospheric Environment*, 32, 1195–1202. https://doi.org/10.1016/S1352-2310(97)00195-7

Hu, X.-M., Klein, P.M., Xue, M., Zhang, F., Doughty, D.C., Forkel, D. et al. (2013) Impact of the vertical mixing induced by low-level jets on boundary layer ozone concentration. *Atmospheric Environment*, 70, 123–130. https://doi.org/10.1016/j.atmosenv.2012.12.046

Jeričević, A. & Grisogono, B. (2006) The critical bulk Richardson number in urban areas: verification and application in a numerical weather prediction model. *Tellus A*, 58, 19–27. https://doi.org/10.1111/j.1600-0870.2006.00153.x

Jones, A.M., Harrison, R.M. & Baker, J. (2010) The wind speed dependence of the concentrations of airborne particulate matter and $NO_x$. *Atmospheric Environment*, 44, 1682–1690. https://doi.org/10.1016/j.atmosenv.2010.01.007

Kalthoff, N., Horlacher, V., Corsmeier, U., Volz-Thomas, A., Kolahgar, B., Geiß, H. et al. (2000) Influence of valley winds on transport and dispersion of airborne pollutants in the Freiburg-Schauinsland area. *Journal of Geophysical Research—Atmospheres*, 105, 1585–1597. https://doi.org/10.1029/1999JD900999

Kalthoff, N., Adler, B., Wieser, A., Kohler, M., Träumner, K., Handwerker, J. et al. (2013) KITcube—a mobile observation platform for convection studies deployed during HyMeX. *Meteorologische Zeitschrift*, 22, 633–647. https://doi.org/10.1127/0941-2948/2013/0542

Kalthoff, N., Lohou, F., Brooks, B., Jegede, G., Adler, B., Babić, K. et al. (2018) An overview of the diurnal cycle of the atmospheric boundary layer during the West African monsoon season: results from the 2016 observational campaign. *Atmospheric Chemistry and Physics*, 18, 2913–2928. https://doi.org/10.5194/acp-18-2913-2018

Kalthoff, N., Adler, B. & Bischoff-Gauss, I. (2020) Spatio-temporal structure of the boundary layer under the impact of mountain waves. *Meteorologische Zeitschrift*, 29, 409–424. https://doi.org/10.1127/metz/2020/1033

Karipot, A., Leclerc, M.Y., Zhang, G., Martin, T., Starr, G., Hollinger, D. et al. (2006) Nocturnal $CO_2$ exchange over a tall forest canopy associated with intermittent low-level jet activity. *Theoretical and Applied Climatology*, 85, 243–248. https://doi.org/10.1029/2007JD009149

Kossmann, M., Vögtlin, R., Corsmeier, U., Vogel, B., Fiedler, F., Binder, H.-J. et al. (1998) Aspects of the convective boundary layer structure over complex terrain. *Atmospheric Environment*, 32, 1323–1348. https://doi.org/10.1016/S1352-2310(97)00271-9

Lamsal, L.N., Martin, R.V. & van Donkelaar, A. (2010) Indirect validation of tropospheric nitrogen dioxide retrieved from the omi satellite instrument: insight into the seasonal variation of nitrogen oxides at northern midlatitudes. *Journal of Geophysical Research—Atmospheres*, 115, 15. https://doi.org/10.1029/2009JD013351

Lareau, N.P., Crosman, E., Whiteman, C.D., Horel, J.D., Hoch, S.W., Brown, W.O.J. et al. (2013) The persistent cold-air pool study. *Bulletin of the American Meteorological Society*, 94, 51–63. https://doi.org/10.1175/BAMS-D-11-00255.1

Lenschow, D.H. & Kristensen, L. (1985) Uncorrelated noise in turbulence measurements. *Journal of Atmospheric and Oceanic Technology*, 11, 68–82. https://doi.org/10.1175/1520-426(1985)002<0068:UNITM>2.0.CO;2

Lenschow, D.H., Wulfmeyer, V. & Senff, C. (2000) Measuring second- through fourth-order moments in noisy data. *Journal of Atmospheric and Oceanic Technology*, 17, 1330–1347. https://doi.org/10.1175/1520-0426(2000)017<1330:MSTFOM>2.0.CO;2

Li, Z., Xiangde, X. & Guoan, D. (2005) Diurnal variations of air pollution and atmospheric boundary layer structure in Beijing during winter 2000/2001. *Advances in Atmospheric Sciences*, 22, 126–132. https://doi.org/10.1007/BF02930876

Löhnert, U. & Crewell, S. (2003) Accuracy of cloud liquid water path from ground-based microwave radiometry 1. Dependency on cloud model statistics. *Radio Science*, 38, 8041. https://doi.org/10.1029/2002RS002654

Löhnert, U., Turner, D. & Crewell, S. (2009) Ground-based temperature and humidity profiling using spectral infrared and microwave observations. Part I: simulated retrieval performance in clear-sky conditions. *Journal of Applied Meteorology and Climatology*, 48, 1017–1032. https://doi.org/10.1175/2008JAMC2060.1

Lohou, F., Kalthoff, N., Adler, B., Babić, K., Dione, C., Lothon, M. et al. (2020) Conceptual model of diurnal cycle of low-level stratiform clouds over southern West Africa. *Atmospheric Chemistry and Physics*, 20, 2263–2275. https://doi.org/10.5194/acp-20-2263-2020

Mahrt, L. (1981) Modelling the depth of the stable boundary layer. *Boundary-Layer Meteorology*, 21, 3–19. https://doi.org/10.1007/BF00119363

Maronga, B., Gross, G., Raasch, S., Banzhaf, S., Forkel, R., Heldens, W. et al. (2019) Development of a new urban climate model based on the model PALM—project overview, planned work, and first achievements. *Meteorologische Zeitschrift*, 28, 105–119. https://doi.org/10.1127/metz/2019/0909

Martucci, G., Milroy, C. & O'Dowd, C.D. (2010) Detection of cloud-base height using Jenoptik CHM15K and Vaisala CL31 ceilometers. *Journal of Atmospheric and Oceanic Technology*, 27, 305–318. https://doi.org/10.1175/2009JTECHA1326.1

Mathieu, N., Strachan, I.B., Leclerc, M.Y., Karipot, A. & Pattey, E. (2005) Role of low-level jets and boundary-layer properties on the NBL budget technique. *Agricultural and Forest Meteorology*, 135, 35–43. https://doi.org/10.1016/j.agrformet.2005.10.001

Mayer, H. (1999) Air pollution in cities. *Atmospheric Environment*, 33, 4029–4037. https://doi.org/10.1016/S1352-2310(99)00144-2

Milroy, C., Martucci, G., Lolli, S., Loaec, S., Sauvage, L., Xueref-Remy, I. et al. (2012) An assessment of pseudo-operational ground-based light detection and ranging sensors to determine the boundary-layer structure in the coastal atmosphere. *Advances in Meteorology*, 18, 929080. https://doi.org/10.1155/2012/929080

Moeng, C.H. (1986) Large-eddy simulation of a stratus-topped boundary layer. Part I: structure and budgets. *Journal of the Atmospheric Sciences*, 43, 2886–2900. https://doi.org/10.1175/1520-0469(1986)043<2886:LESOAS>2.0.CO;2

Newman, J.F., Klein, P.M., Wharton, S., Sathe, A., Bonin, T.A., Chilson, P.B. et al. (2016) Evaluation of three lidar scanning strategies for turbulence measurements. *Atmospheric Measurement Techniques*, 9, 1993–2013. https://doi.org/10.5194/amt-9-1993-2016

Ohya, Y., Nakamura, R. & Uchida, T. (2008) Intermittent bursting of turbulence in a stable boundary layer with low-level jet. *Boundary-Layer Meteorology*, 126, 349–363. https://doi.org/10.1007/s10546-007-9245-y

Panday, A.K. & Prinn, R.G. (2009) Diurnal cycle of air pollution in the Kathmandu Valley, Nepal: observations. *Journal of Geophysical Research—Atmospheres*, 114, D09305. https://doi.org/10.1029/2008JD009777

Pardyjak, E.R., Fernando, H.J.S., Hunt, J.C., Grachev, A.A. & Anderson, J. (2009) A case study of the development of

nocturnal slope flows in a wide open valley and associated air quality implications. *Meteorologische Zeitschrift*, 18, 85–100. https://doi.org/10.1127/0941-2948/2009/362

Pisano, J.T., McKendry, I., Steyn, D.G. & Hastie, D.R. (1997) Vertical nitrogen dioxide and ozone concentrations measured from a tethered balloon in the Lower Fraser Valley. *Atmospheric Environment*, 31, 2071–2078. https://doi.org/10.1016/S1352-2310(96)00146-X

Price, J.D., Vosper, S., Brown, A., Ross, A., Clark, P., Davies, F. et al. (2011) COLPEX: field and numerical studies over a region of small hills. *Bulletin of the American Meteorological Society*, 92, 1636–1650. https://doi.org/10.1175/2011BAMS3032.1

Reitebuch, O., Strassburger, A., Emeis, S. & Kuttler, W. (2000) Nocturnal secondary ozone concentration maxima analysed by sodar observations and surface measurements. *Atmospheric Environment*, 34, 4315–4329. https://doi.org/10.1016/S1352-2310(00)00185-0

Rose, T., Crewell, S., Löhnert, U. & Simmer, C. (2005) A network suitable microwave radiometer for operational monitoring of the cloudy atmosphere. *Atmospheric Research*, 75, 183–200. https://doi.org/10.1016/j.atmosres.2004.12.005

Rotach, M.W., Gohm, A., Lang, M.N., Leukauf, D., Stiperski, I. & Wagner, J.S. (2015) On the vertical exchange of heat, mass, and momentum over complex, mountainous terrain. *Frontiers in Earth Science*, 3, 76. https://doi.org/10.3389/feart.2015.00076

Salmond, J.A. & McKendry, I.G. (2002) Secondary ozone maxima in a very stable nocturnal boundary layer: observations from the Lower Fraser Valley, BC. *Atmospheric Environment*, 36, 5771–5782. https://doi.org/10.1016/S1352-2310(02)00698-2

Sanchez, M.L., de Torre, B., Garcia, M.A. & Pérez, I. (2007) Ground-level ozone and ozone vertical profile measurements close to the foothills of the Guadarrama Mountain range (Spain). *Atmospheric Environment*, 41, 1302–1314. https://doi.org/10.1016/j.atmosenv.2006.09.047

Scherer, D., Florian, A., Bender, S., Cortekar, J., Emeis, S., Fehrenbach, U. et al. (2019a) Urban Climate Under Change $[UC]^2$—a national research programme for developing a building-resolving atmospheric model for entire city regions. *Meteorologische Zeitschrift*, 28, 95–104. https://doi.org/10.1127/metz/2019/0913

Scherer, D., Ament, F., Emeis, S., Fehrenbach, U., Leitl, B., Scherber, K. et al. (2019b) Three-dimensional observation of atmospheric processes in cities. *Meteorologische Zeitschrift*, 28, 121–138. https://doi.org/10.1127/metz/2019/0911

Sørensen, J.H., Rasmussen, A., Ellermann, T. & Lyck, E. (1998) Mesoscale influence on long-range transport, evidence from ETEX modelling and observations. *Atmospheric Environment*, 32, 4207–4217. https://doi.org/10.1016/S1352-2310(98)00183-6

Steyn, D.G., De Wekker, S.F.J., Kossmann, M. & Martilli, A. (2013) Boundary layers and air quality in mountainous terrain. In: Chow, F.K., De Wekker, S.F.J. & Snyder, B.J. (Eds.) *Mountain weather research and forecasting: recent Progress and current challenges*. Dordrecht, The Netherlands: Springer, pp. 261–289 ISBN 978-94-007-4098-3.

Stull, R.B. (1988) *An introduction to boundary layer meteorology*. Dordrecht, NL: Kluwer Academic Publication.

Vogelezang, D.H.P. & Holtslag, A.A.M. (1996) Evolution and model impacts of alternative boundary layer formulations. *Boundary-Layer Meteorology*, 81, 245–269. https://doi.org/10.1007/BF02430331

Wang, L., Wang, J., Tan, X. & Fang, C. (2020) Analysis of $NO_x$ pollution characteristics in the atmospheric environment in Changchun City. *Atmosphere*, 11, 30. https://doi.org/10.3390/atmos11010030

Wanner, H. & Hertig, J.-A. (1984) Studies of urban climates and air pollution in Switzerland. *Journal of Applied Meteorology and Climatology*, 23, 1614–1625. https://doi.org/10.1175/1520-0450(1984)023<1614:SOUCAA>2.0.CO;2

Wetzel, P.J. (1982) Toward parameterization of the stable boundary layer. *Journal of Applied Meteorology*, 21, 7–13. https://doi.org/10.1175/1520-0450(1982)021<0007:TPOTSB>2.0.CO;2

Whiteman, C.D., Bian, X. & Zhong, S. (1999) Wintertime evolution of the temperature inversion in the Colorado Plateau Basin. *Journal of Applied Meteorology*, 38, 1103–1117. https://doi.org/10.1175/1520-0450(1999)038<1103:WEOTTI>2.0.CO;2

Wittkamp, N., Adler, B., Kalthoff, N. & Kiseleva, O. (2021) Mesoscale wind patterns over the complex urban terrain around Stuttgart investigated with dual-Doppler lidar profiles. *Meteorologische Zeitschrift*, 30, 185–200. https://doi.org/10.1127/metz/2020/1029

Zardi, D. & Whiteman, C.D. (2013) Diurnal mountain wind systems. In: Chow, F.K., De Wekker, S.F.J. & Snyder, B.J. (Eds.) *Mountain weather research and forecasting: recent Progress and current challenges*. Dordrecht, The Netherlands: Springer, pp. 35–119 ISBN 978-94-007-4098-3.

Zhong, S. & Fast, J. (2003) An evaluation of the MM5, RAMS, and Meso-eta models at subkilometer resolution using VTMX field campaign data in the salt Lake Valley. *Monthly Weather Review*, 131, 1301–1322. https://doi.org/10.1175/1520-0493(2003)131%3c1301:AEOTMR%3e2.0.CO;2

**How to cite this article:** Kiseleva, O., Kalthoff, N., Adler, B., Kossmann, M., Wieser, A., & Rinke, R. (2021). Nocturnal atmospheric conditions and their impact on air pollutant concentrations in the city of Stuttgart. *Meteorological Applications*, *28*(6), e2037. https://doi.org/10.1002/met.2037

## APPENDIX A: THRESHOLDS FOR CRITICAL VALUES OF Rib

Some ambiguity concerning the critical value of the Richardson number, Ribc, exists in the literature. For example, an empirically determined Ribc value for the convective boundary layer (CBL), that is, below which the flow is deemed to be dynamically unstable, is 0.25 according to Stull (1988) and Sørensen et al. (1998) and is 0.22 according to Beyrich and Leps (2012) and Jeričević

and Grisogono (2006). For stable, nocturnal atmospheric conditions, a wide range of Ribc values is used in practice, ranging from 0.3 (Vogelezang & Holtslag, 1996), to 0.33 (Banta, 2008; Wetzel, 1982), and 0.5–1.0 (Mahrt, 1981) to 1.5 (Jeričević & Grisogono, 2006). The low value of 0.33 is often used in models (Collaud Coen et al., 2014; Kalthoff et al., 2020), and the large value of Jeričević and Grisogono (2006) was derived for an urban environment, which they attributed to the enhanced surface roughnesses of cities. Wittkamp et al. (2021) found an Ribc value of 1.25 for Stuttgart, which separates dynamically unstable flows, during which the flow in the Neckar valley was coupled to the flow aloft, from dynamically stable flows, during which the two flows were decoupled. In the case of decoupling, the flow in the valley was mainly channelled in along-valley direction.

## APPENDIX B: CRITERION FOR THE DEFINITION OF LOW CLOUDS WITH MODERATE AND STRONG WIND SPEED

The separation between low clouds with moderate and strong wind is done using a threshold which is given by the mean wind speed plus standard deviation calculated for the low-cloud cases in summer (e.g., $5.3 \pm 3.0$ m s$^{-1}$ at 200 m agl). Summer data were used for threshold calculation in order to separate winter cases into those with wind speeds that are comparable to the summer cases and to those that are considerably higher. The winter cases with a wind speed that is below (above) the threshold are denoted as moderate (strong) wind-speed cases (abbreviated as LC1 and LC2, respectively).